Geothermics 136 (2026) 103620

Contents lists available at ScienceDirect

Geothermics

journal homepage: www.elsevier.com/locate/geothermics

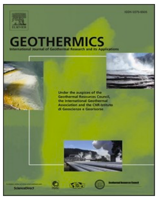

Direction-dependent permeability and resistivity of fractured rocks tuned to New Zealand geothermal reservoirs

Alison Kirkby [*], Cécile Massiot

Earth Sciences New Zealand Wairakei Research Centre, New Zealand

ARTICLE INFO

Keywords:
Permeability
Resistivity
Faults
Fractures
Numerical model

ABSTRACT

Understanding permeability in the Earth is vital to optimizing sustainable geothermal development. In many geothermal fields, permeability is controlled by faults, resulting in high spatial and directional variability, difficult to characterise without costly drilling. Electrical resistivity, however, can be measured from the surface, and like permeability, is sensitive to fluids if they are sufficiently conductive. Modelling of resistivity-based geophysical data has largely focussed on isotropic properties to map clay caps and deep heat sources. However, faults commonly have a preferred orientation, and fluid-filled faults often have lower resistivity than the matrix, so anisotropy of permeability and resistivity is expected. This study models faults from the borehole to field scale to characterise direction-dependent permeability and resistivity. Parameters are derived from active faults and geothermal fields in the Taupō Volcanic Zone (TVZ), New Zealand. In our base-case model, permeability is highest (6×10^{-13} m^2) in the horizontal along-dominant-strike direction, lower vertically (5×10^{-14} m^2), and lowest in the across-dominant strike direction (2×10^{-14} m^2), with significant uncertainty in across-strike permeability (4×10^{-15} m^2 to 5×10^{-14} m^2). For typical TVZ fluids (0.5 Ωm) and 1000 Ωm matrix, resistivity is lowest along dominant strike (235 Ωm), slightly higher vertically (285 Ωm) and highest across-strike (575 ± 30 Ωm). Resistivity anisotropy ratios along-strike/across-strike are relatively consistent regardless of fault length distribution (~0.38–0.5), but vary strongly with the proportion of along-strike faults. Anisotropy ratios for permeability are more variable (1–300). The calculated petrophysical properties help link reservoir models with geophysical data, which may guide fractured reservoir models and resource use.

Plain language summary

Understanding how easily water can move underground (i.e. permeability) is important for using resources like groundwater and geothermal in an economic and sustainable way. In many geothermal areas, like those in New Zealand's Taupō Volcanic Zone (TVZ), permeability is mostly controlled by faults, or cracks, within the Earth. These vary in size and direction and can be difficult to find.

Scientists can measure Earth's electrical resistivity to study geothermal areas and work out where to drill with the best chance of finding permeable zones. To simplify these models, they normally assume the properties are the same in all directions. However, faults tend to line up in certain directions and contain fluids that affect resistivity, both the resistivity and the ability of the rock to flow fluids can change depending on the direction they are measured.

This study uses numerical models to look at how faults affect permeability and resistivity at a range of scales. The results show that permeability is highest along the main fault direction, lower vertically, and lowest across the faults. Resistivity also changes with direction, with resistivity along the main fault direction about a third to half that across the faults.

1. Introduction

Rock permeability is essential for the extraction and recharge of Earth resources such as groundwater and geothermal, as well as hydrothermal and volcanic systems. Reservoir permeability is often controlled by fractures and faults (McNamara et al., 2015; Bolós et al., 2019; Intani et al., 2020; Jolie et al., 2021; Liotta et al., 2021). In these cases, the density, orientation and connectivity of open faults are key considerations in designing drilling strategies to extract fluids.

Resistivity-based geophysical methods such as magnetotellurics (MT) are applied to understand geothermal resources. They are highly sensitive to the clay alteration zone that commonly overlies the reservoir and deep heat sources (e.g., Bibby et al., 1995, Bertrand et al., 2013, Lee

---

[*] Corresponding author.
E-mail address: a.kirkby@gns.cri.nz (A. Kirkby).

https://doi.org/10.1016/j.geothermics.2026.103620
Received 7 October 2025; Received in revised form 20 January 2026; Accepted 31 January 2026

et al., 2020, Ardid et al., 2021, Bertrand et al., 2022, Ishizu et al., 2022, Yamaya et al., 2022). Key information that is often missing is the distribution and orientation of open fractures within the reservoir or upflow zone. Interpretation of acoustic and micro-resistivity borehole images often shows that faults and fractures inferred to be open commonly show a preferred orientation (e.g. Dezayes et al., 2010, McNamara et al., 2015, Vidal et al., 2016, Massiot et al., 2017, McNamara et al., 2019, Ikhwan et al., 2020, Milicich et al., 2023). Reservoir observations (e.g. Calibugan et al., 2022) and discrete fault network models (Kissling and Massiot, 2023) suggest that bulk permeability is also anisotropic. However, information on fault orientations, and implications for permeability, is normally not known until after several wells have been drilled. Seismic anisotropy has shown promise in constraining fault orientations (e.g., Mroczek et al., 2020, Jylhänkangas, 2024) although such data does not directly image the connectivity of fluids.

Although resistivity is a direction dependent property, published resistivity models are largely isotropic, mainly because the number of parameters to be solved is already far larger than the number of data, and in most cases, it is possible to find an isotropic model that has an adequate fit to the data. However, electrical resistivity can vary with orientation, both on a micro-scale (due to the alignment of mineral grains) and a macro scale (due to bedding or aligned faults or faults) (Wannamaker, 2005; Martí, 2014). In the case of geothermal reservoirs containing faults filled with fluids, macro-anisotropy in resistivity may be directly related to the alignment of permeable structures. Indeed, fluids contained in open faults are normally more conductive than the rock matrix. Although conductive clay minerals are abundant in the lower-temperature (<200 °C) parts of the hydrothermal system, these generally transition to more resistive clays and crystalline minerals at high temperatures (Browne, 1970; Muraoka et al., 1998; Simmons and Browne, 2000; Franzson et al., 2008; Jolie et al., 2021). Conductive sulphide minerals such as pyrite can occur at rates of up to a few percent locally which may influence the host rock resistivity (Simmons and Browne, 2000; Wallis et al., 2009). However, on a field scale, overall concentrations tend to be small (~1%) limiting the impact of these phases on the overall resistivity and particularly any direction dependence of resistivity (Simmons and Browne, 2000). Thus, attributes of the resistivity tensor (orientation, and relative magnitude of the components) could be a key piece of information in understanding the permeability structure of a reservoir controlled by fluid-filled faults.

The permeability of fractures and faults has been measured on the sub-metre scale (Watanabe et al., 2008; Watanabe et al., 2009; Ishibashi et al., 2015; Heap and Kennedy, 2016), but there are far fewer measurements of fault permeability on the reservoir scale. Instead, bulk reservoir permeability is usually determined in the calibration of numerical reservoir models (Kaya et al., 2014; Tateishi et al., 2015; O'Sullivan et al., 2025). Resistivity of individual faults has been measured, although this is done less often than permeability (Sawayama et al., 2021a; Sawayama et al., 2023). At the reservoir scale, resistivity is inferred from inversion of MT data, although this is typically assumed isotropic, and uncertain due to non-uniqueness, particularly in the typical geothermal scenario where a conductive clay cap overlies the reservoir, reducing sensitivity to structures below this. Downhole resistivity measurements are limited in geothermal fields and focused on isotropic resistivity (Muraoka et al., 1998; Wallis et al., 2009; Mortensen et al., 2014), while downhole resistivity anisotropy tools are sometimes used in hydrocarbon reservoirs (Hou et al., 2016). Petrophysical modelling has the potential to link lab- and reservoir scales, and the evolution of the relationship between permeability and resistivity between these two scales.

This paper aims to link permeability estimated at the core scale to that at reservoir scale, and then link these permeability estimates to core and reservoir-scale resistivity. Models of (1) individual faults and then (2) fault networks, are constructed using parameters from field data in geothermal fields of New Zealand's Taupō Volcanic Zone. A particular focus of the resulting models will be the anisotropy in both resistivity and permeability that is expected at the reservoir scale.

2. Background

2.1. *Models of fault permeability and resistivity*

Numerical modelling shows resistivity and permeability of faults and fault networks display a percolation threshold, i.e., both properties are low at small apertures and then change over many orders of magnitude at a point when the faults become fully connected through the domain (Bahr, 1997; Kirkby et al., 2016; Kirkby and Heinson, 2017; Kissling and Massiot, 2023). However, the increase in connectivity with increasing volume fraction is normally more gradual for resistivity than it is for permeability, reflecting a less sharply defined percolation threshold (Kirkby et al., 2016; Kirkby and Heinson, 2017).

Laboratory measurements of individual faults at variable normal stresses are consistent with permeability and resistivity at or just above the percolation threshold, with permeability on individual faults typically around 10^{-12} to 10^{-13} m^2 on faults with no displacement, and 10^{-9} to 10^{-8} m^2 on faults with 3–5 mm displacement (Watanabe et al., 2008; Watanabe et al., 2009; Ishibashi et al., 2015; Sawayama et al., 2023).

The fraction of these measured faults that has both planes in contact covers a relatively narrow range of 35–42% for faults with >1 mm displacement, which is near constant with pressure, at pressures from 10–100 MPa (Watanabe et al., 2008; Watanabe et al., 2009; Ishibashi et al., 2015). For faults with 0–1 mm displacement, contact areas increase more strongly with pressure from 31–66%. Thus, faults should be modelled with realistic contact area ratio to produce realistic fracture properties.

A challenge of modelling fault flow properties is balancing small cell sizes needed to capture fluid flow effects of sub-mm scale fault roughness against modelling large enough areas/volumes to represent the scale of interest. Due to the minimum cell sizes of <1 mm needed to model fault roughness, the typical scale of simulation is limited to tens of cm to metre-scale (Ishibashi et al., 2015; Kirkby et al., 2016; Kirkby and Heinson, 2017; Sawayama et al., 2021a). However, estimating resistivity and permeability at the scale of a geothermal reservoir requires faults at scales of centimetres to tens of metres or more. While fault size, on its own, does not impact resistivity and permeability (Ishibashi et al., 2015; Sawayama et al., 2023), the displacement on faults increases with fault size (Kim and Sanderson, 2005). For normal faults, this increase is broadly linear on a log scale, with slope ~ 1; i.e., displacement is a constant fraction of size (Kim and Sanderson, 2005). As displacement on a fault grows, opposing surfaces become increasingly mismatched, leading to an increase in the size of asperities on the fault, increased space for fluids and thus an increase in permeability and decrease in resistivity (Sawayama et al., 2023). These larger asperities are likely to dominate both current and fluid transport properties over any fine scale roughness caused by sub-mm scale mismatching on the fault planes, allowing cell size to be increased for larger faults with larger displacements (Section S1).

2.2. *Taupō volcanic zone*

To focus this study, and enable direct comparison to observations, model parameters were selected based on characteristics of the Taupō Volcanic Zone (TVZ), New Zealand (Fig. 1), that has been extensively studied. The TVZ has been the site of geothermal energy production for electricity for >50 years and currently provides nearly 20% of New Zealand's electricity (MBIE, 2025). The TVZ is Hikurangi Subduction Zone's volcanic arc (Wilson et al., 1995). The Taupō Rift is an intra-arc rift where the extension coincides with the TVZ (Wilson and Rowland, 2016; Villamor et al., 2017). The modern Taupō Rift is a 15 – 40 km wide zone of closely spaced faults, dominated by steeply-dipping normal faults (Nicol et al., 2006; Seebeck et al., 2014; Villamor et al., 2017;

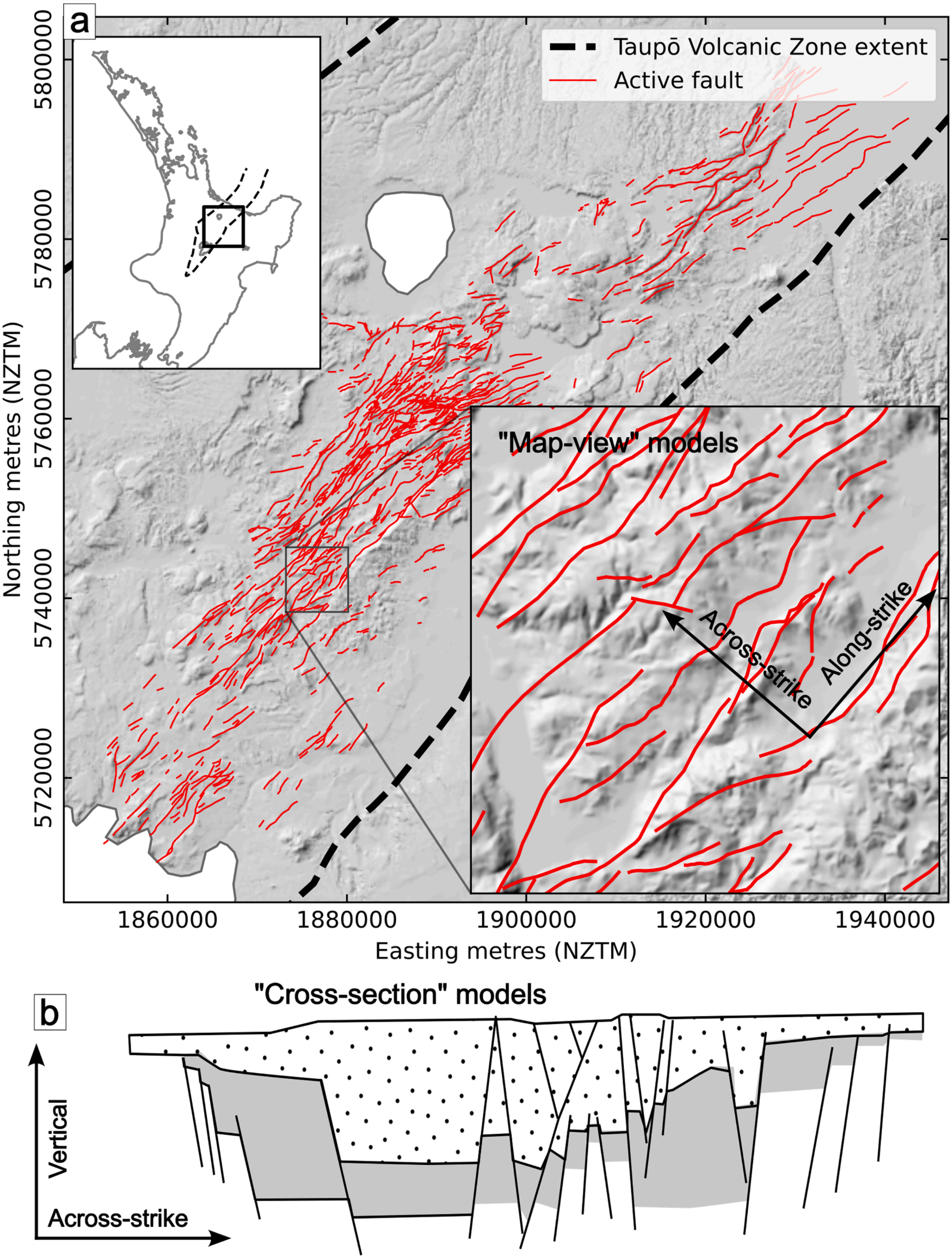

Fig. 1. Representative (a) map-view and (b) cross-section of normal faults antithetic and synthetic splays, that occur in the TVZ from geothermal field to rift scales. Insert of (a) shows the location of the TVZ in the North Island of New Zealand. Active faults after Morgenstern et al. (2025); and TVZ extent after Wilson et al. (1995); the synthetic cross-section is modified after Villamor et al. (2017) and McNamara et al. (2019) and applies to either field- or rift-scales. Topography from LINZ (2012).

Seebeck et al., 2024; Morgenstern et al., 2025). In geothermal fields, numerous studies have characterised fractures and faults using borehole images (Wallis et al., 2012; McNamara et al., 2015, 2019; Massiot et al., 2017, 2023, 2025; Milicich et al., 2023; Wallis, 2023; Morgenstern et al., 2025), fault systems using stratigraphic offsets (Chambefort et al., 2014; Milicich et al., 2014, 2020; Rosenberg, 2017), fluid composition and temperature (Hedenquist, 1983, 1990; Chambefort et al., 2016; McNamara et al., 2016; Mroczek et al., 2016). In addition, electrical resistivity has been measured based on DC resistivity, MT, and airborne electromagnetic data (Bibby et al., 1995; Heise et al., 2008; Bertrand et al., 2013, 2015, 2022; Heise et al., 2016; Reeves and Pederson, 2023).

3. Method

This study employs a three-stage, 2D approach. First, we estimate fault resistivity and permeability capturing fine-scale fault roughness (Fig. 2). Secondly, we compute resistivity of a small-scale faulted volume, and then finally upscale to reservoir scale.

3.1. Individual fault models

The first step is to apply the approach of Kirkby et al. (2016) to estimate permeability and resistivity for individual faults of different sizes (Fig. 2a-b, f-g), with a modification to the permeability calculation (Section S2). This method is discussed in detail in Kirkby et al. (2016) and so only a summary is provided here. The approach is implemented in Python and the code is available (Kirkby, 2026). First, a pair of synthetic square fault surfaces are generated based on characteristics of real faults (Brown, 1995; Matsuki et al., 2006). They are then displaced parallel to the fracture plane by a desired amount (i.e. the top surface is translated along the fault plane). Resolution of the fault is determined as 10% of displacement, to a minimum of 0.1 mm, which is adequate to accurately model the properties of the faults (Section S1). The fault planes are then shifted apart or together until they reach a target percentage of contact area. Regions with overlapping or very small apertures are set to a minimum value of 1 μm (Watanabe et al., 2008) to account for sub-μm roughness causing asperities at contact points.

The resistivity and permeability of the faults are then modelled in two directions, parallel and perpendicular to the displacement direction assuming faults are fully saturated with reservoir fluid. Resistivity and permeability are modelled, respectively, by Ohm's law and Darcy's Law, with each cell in the fracture plane having a local permeability and resistivity computed from analytical solutions for a conductive fluid in a wedge (Brush and Thomson, 2003; Kirkby et al., 2016). Fluid resistivity is discussed in Section 3.3.1. The models have a pressure gradient and voltage applied along the length of the fault, i.e. constant pressure and voltage boundary conditions on each end of the fault, and no-flow boundary conditions at the sides (Brown, 1989; Nicholl et al., 1999; Brush and Thomson, 2003; Kirkby et al., 2016). The total fluid and current passing through the fault are then used with Darcy's Law and Ohm's Law to respectively compute the overall permeability and resistivity of the fault. This process is carried out in faults with thirteen displacement values, ranging from zero to 50 cm (approximately evenly in log space), later linked to fault length (Section 3.3.1). For each fault, the opposing surfaces are progressively shifted apart and modelled at 30 unique proportions of contact area (0.10 to 0.68), with 96 repeats for

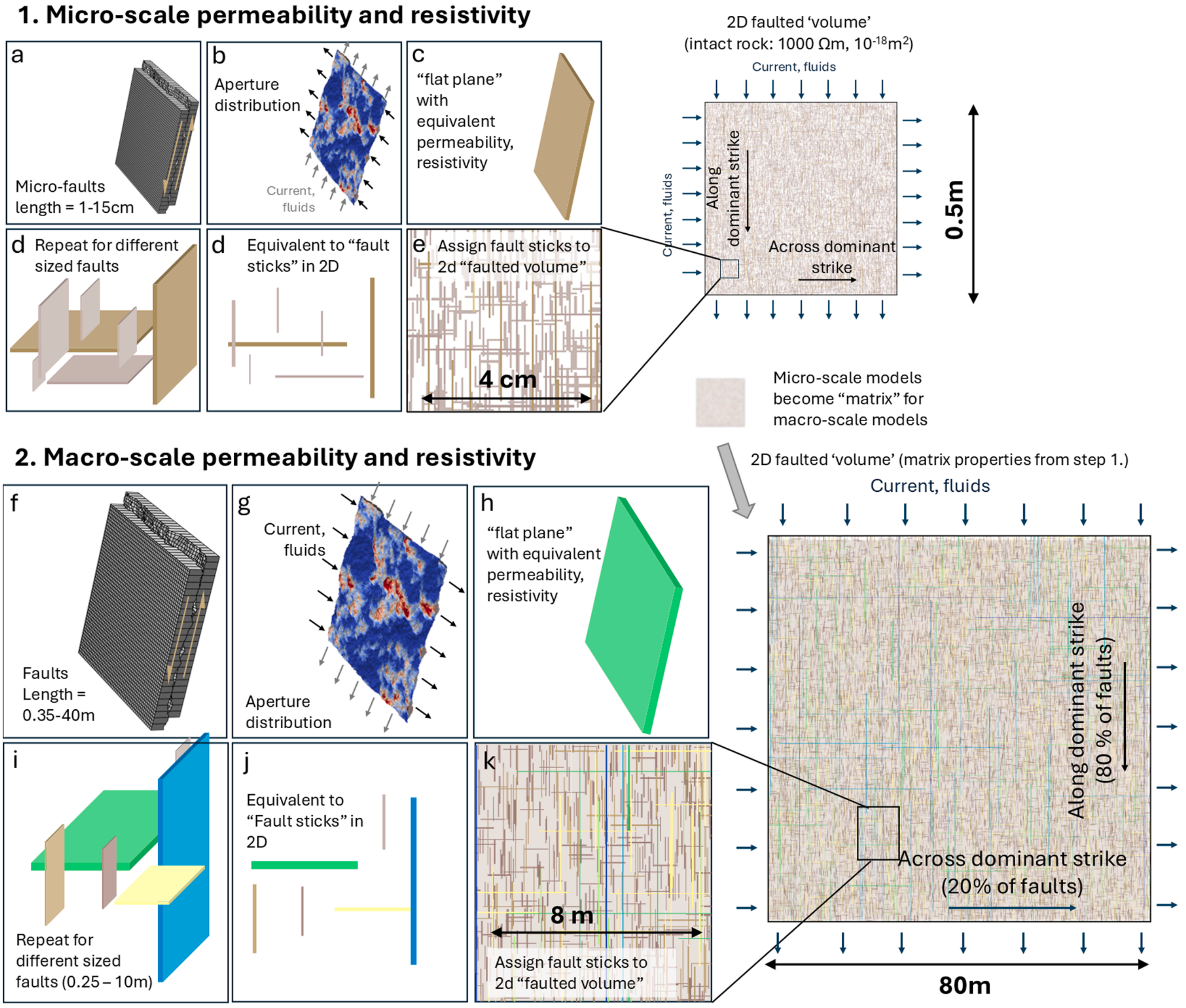

Fig. 2. Diagram illustrating the multi-scale approach employed in this study to model the permeability of a faulted volume. The 2d "fault volume" models represent a map-view, when considering a TVZ-like (extensional) regime, with vertical fault displacement and the dominant strike along the rift axis. Explain a-k.

each displacement value. From these models, a subset was selected that were within the range of contact area as discussed in Section 3.3.1.

The resulting fault permeability and resistivity values for each model are provided in both directions, i.e. perpendicular and parallel to displacement. Fault resistivity is defined here as the equivalent resistivity of a hypothetical, uniformly thick sheet that represent the actual fault (Fig. 2c-d, h-i). The sheet has a constant width equal to the mean aperture of the fault, and its resistivity is computed such that it preserves the same overall electrical response as the original fault.

To pass the resulting permeability and resistivity distributions through to models of a faulted volume, the resistivity and hydraulic aperture of the equivalent "sheet" is translated to its cross-sectional equivalent, a "fault stick" (Fig. 2d, j). This allows fault resistivities to be passed into macro-scale models of faulted volumes, as uniformly thick sticks. The parameters used for the models are discussed in Section 3.3.

3.2. Fault stick models

Individual fault permeabilities and resistivities are then used in 2D "fault stick" models (Kissling and Massiot, 2023) (Fig. 2). The fault sticks are placed in one of two orthogonal directions. Fault hydraulic aperture and resistivity values are assigned using the results of step (1) (Section 3.1). In these models, the relative proportions of faults of different sizes, and proportions in the direction along the dominant strike direction (P_z), are set based on field measurements (Section 3.3; Table 1). The models predict bulk permeabilities and resistivity in two directions.

Fault stick models are generated on two embedded scales: first, 0.5 m x 0.5 m models, containing faults $\leq$ 0.2 m in length, are used to assess permeability, porosity and resistivity associated with small-scale faults. These are termed "micro-faults". Next, models 80 m x 80 m in area were constructed containing faults from 0.3 to 50 m in length. The matrix properties in these models was set as permeability and resistivity from the smaller scale models (Fig. 2).

As a 3-dimensional proxy, two sets of 2-D fault stick models were generated. In the first set ("map view") (Fig. 1), fault permeabilities and resistivities are defined using individual-fault models (Section 3.1) where these properties were modelled perpendicular to slip. In a "TVZ-like" regime, dominated by near-vertical normal faults (e.g. McNamara et al., 2019), the two directions are horizontal, aligned along the dominant strike (NE-SW) and across the dominant strike (NW-SE). We herein refer to these directions as "along-strike" and "across-strike". In the second set of models ("cross-section view"), fault permeabilities and resistivities parallel to slip were used. These are representative of vertical cross-sections oriented NW-SE, i.e. comprising a majority of vertical faults and a minority of horizontal faults. The two directions are "vertical" and horizontal across the dominant fault strike ("across--strike"). This second set is similar to models of Kissling and Massiot (2023).

The two "across-strike" models represent the same direction (NW-SE) but will have different permeabilities, due to using fault permeability parallel to slip in the "cross-section view" models and perpendicular to slip in the "map-view" models. This discrepancy could be addressed by modelling fault volumes in 3D The permeability in the direction across the dominant strike will likely be intermediate between the two models and will depend on the true direction of fault displacement.

3.3. Parameter selection

3.3.1. Models of individual faults

The displacement magnitude on individual faults was scaled with fault length using constant fraction of 0.01 (Kim and Sanderson, 2005), with faults smaller than 0.1 m assumed to have no displacement. This generates asperities that increase in size with fault length. Models had a minimum fault length of 1 cm, and a maximum length of 50 m, i.e. 0.5 m displacement. The upper limit to scale is driven by the assumption of no deformation/gouge formation on the fault plane, which is likely to become invalid for larger fault displacements.

The roughness of fault surfaces can be characterised by an amplitude parameter and fractal dimension D, which controls the relative roughness on a large to small scale (Brown, 1995). Amplitude of surface heights can be defined in terms of scaling factor s, which relates the standard deviation of surface heights of a reference fault, $\sigma_{h,\ ref}$ to its length L_{ref} and fractal dimension D (Matsuki et al., 2006; Kirkby et al., 2016):

$$s = \frac{\sigma_{h,\ ref}}{L_{ref}^{(3\ -\ D)}} \tag{1}$$

Increasing fractal dimension has minimal effect on flow and resistivity, while increasing scaling factor increases permeability and reduces resistivity (Sawayama et al., 2023). Measurements on core samples on a variety of lithologies suggest natural faults tend to have lower scaling factors, and slightly higher fractal dimensions, than

Table 1
Summary of parameters used in models.

Individual fault parameters							
	Base case scenario	Single parameter sensitivity analysis					
Length (L)	0.01 – 50 m (13 fault lengths). Faults with length < 0.1 m were given same properties as 0.1 m faults.	As base case					
Cell size	d / 10 to a minimum of 0.1 mm	As base case					
Displacement (d)	0.01 x L	As base case					
Fractal dimension	2.34	As base case					
Scaling factor	0.0017	As base case					
Area of contact between fault planes (inter-quartile ranges from Fig. 2c)	56–63% ($d = 0$ mm) 47–56% ($d = 1$–2 mm) 34–43% ($d \geq 3$ mm)	As base case					
Fluid resistivity (ρ_f)	0.5 Ωm	0.01 to 50					
Matrix resistivity	1000 Ωm	As base case					
Matrix permeability	10^{-18} m^2	As base case					
Number of repeats	96 for each displacement	As base case					
Fault network parameters							
Cell size	0.5 mm (0.5 m x 0.5 m model) 0.05 m (80 m x 80 m model)	As base case					
Fault density exponent (γ)	3.1	2.9	3.0	3.1	3.1	3.2	3.3
Fracture porosity	1.5%	1.5%	1.5%	1%	2%	1.5%	1.5%
Fault density constant α	2.37	4.34	3.29	1.58	3.15	2.18	1.47
Proportion along-strike / vertical faults (Pz)	0.8	0.7, 0.8, 0.9, 0.95, 0.98, 0.99, 1.0					
Number of repeats	100 for each parameter set	As base case					

induced faults created in the lab (Fig. 3), which may reflect deformation on the fault plane during the natural fracture generation and slip process. Based on these measurements, we set $D = 2.34$ and $s = 0.0017$.

Ranges for percentage contact area between fault planes were chosen based on the 25th and 75th percentile from measurements at 20 to 100 MPa (Watanabe et al., 2008, 2009; Nemoto et al., 2009; Ishibashi et al., 2015) (Fig. 3C). This corresponds to 56–63% for faults with zero displacement, 47–56% for those with 1–2 mm displacement and 34–43% for $\geq$3 mm displacement (Watanabe et al., 2008, 2009; Nemoto et al., 2009; Ishibashi et al., 2015).

Fluid resistivity is estimated from salinity and temperature. The resistivity of water decreases with increasing temperature and concentration of dissolved ions (e.g. Bannard, 1975; Ucok et al., 1980; Watanabe et al., 2022). A representative NaCl content of 2000 ppm was estimated based on estimates of parent fluid Cl^- concentration ranging from 1069 – 1400 ppm at Ngatamariki, Ohaaki, and Rotokawa geothermal fields in the TVZ (Hedenquist, 1983, 1990; Chambefort et al., 2016; Mroczek et al., 2016). This concentration with a reservoir temperature of 280 °C (Chambefort et al., 2016; McNamara et al., 2016; Mroczek et al., 2016) gives a fluid resistivity of $\sim$0.5 Ωm (Watanabe et al., 2022). To explore the changes in bulk resistivity as fluid resistivity is changed, several additional fluid resistivities were considered, ranging from 0.01 to 500 Ωm. Intact rock (matrix) resistivity is set to 1000 Ωm.

3.3.2. *Fault network parameters*

The density of different sized faults can be described by a power law distribution (Bonnet et al., 2001), with the number of faults greater than a given size (N_f) given in terms of a density constant α and exponent γ:

$$N_f = \frac{\alpha}{1-\gamma} l_{min}^{1-\gamma} R^2 \tag{2}$$

Here, the exponent was determined based on analysis of a vein dataset collected on exposed basement rocks like those found in the deep TVZ (Massiot et al., 2025), with a best fit value of 3.1 (Section S3). A similar analysis on the active fault database in the TVZ gives a value of 3.6. Since the outcrop dataset is at a more similar scale to our models, we use a base case scenario of γ=3.1 but model a range of values (Table 1) to accommodate uncertainties in the outcrop dataset.

If γ and the aperture/volume of each fault is known, then the density constant α and the fault porosity are directly linked, i.e. choice of one parameter implies the other. In measured fault systems, α spans seven orders of magnitude (Bonnet et al., 2001).

The fracture porosity (i.e. the total volume of pore open space within due to fractures) in natural geothermal systems in the TVZ has been inferred at several scales of observation. Borehole images at the Rotokawa and Kawerau geothermal fields suggest a porosity of around 4–10% including large faults, open fractures and filled veins (Massiot et al., 2017). A similar combined vein and fracture connected porosity (4–10%) was found in thin sections (Siratovich et al., 2014; Wyering et al., 2014; Cant et al., 2018). Therefore, the open fault connected porosity is <4–10%. Microscale fault network models result in a connected porosity from open faults of $\sim$2% at the percolation threshold (Kirkby and Heinson, 2017). Similar estimations of open fracture porosity were found through synthetic forward modelling of open faults to match seismic anisotropy responses (2.5% and 4.5% respectively, for the Ngatamariki and Rotokawa geothermal fields) (Jylhänkangas, 2024). Models presented here include a base scenario (1.5%) and two additional scenarios with fracture porosity of 1% and 2% (Table 1). Higher porosities were trialled but gave unrealistically high permeabilities.

Finally, the proportion of faults in each orthogonal direction was estimated separately for the “map-view” and “cross-section” models, both returning $\sim$0.8, i.e. 80% of the total faults are aligned parallel to strike and 20% perpendicular. This parameter is termed P_z, i.e. the proportion of faults in the dominant strike direction. For the “map view” models, P_z was estimated based on a length-weighted average of the strike-parallel component of fault segments from the Taupō Rift in New Zealand’s active fault database (Morgenstern et al., 2025), relative to the total length of faults in this region (Supplementary Section S4).

For the vertical direction, P_z was computed using fault and fracture dip magnitudes interpreted from borehole images at the Rotokawa and Wairakei geothermal fields (Massiot et al., 2017; McNamara et al., 2019). Borehole images do not inform on fault length, so each fault was weighted as if it had the same length. Borehole image-derived P_z is similar to that calculated from active faults (0.79). Thus a value of 0.8 was used to define the relative proportion of faults along and across the dominant strike, for both the “map view” and “cross-section” sets of fault models.

Fault centres and orientations were assigned randomly while matching P_z. To test the sensitivity of the models to P_z, a range of values was tested from 0.7 to 0.99.

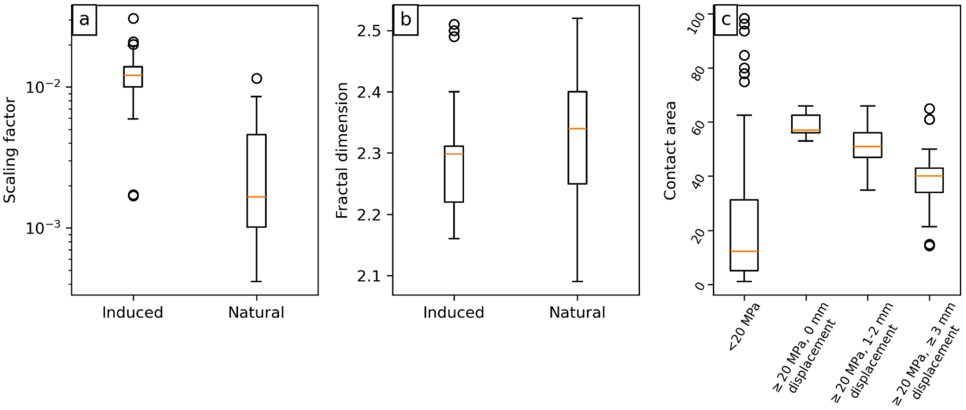

Fig. 3. Box and whisker plots of published data for (a) scaling factor, (b) fractal dimension, and (c) contact area proportion on faults and fault surfaces. The orange bars represent the median, and the boxes show the range from the 1st to 3rd quartile. The whiskers are shown at the furthest data point lying within 1.5 times the inter-quartile range from the box, with points outside that range shown as circles. Data from (a) and (b) from the following sources: (Brown and Scholz, 1986; Chen and Spetzler, 1993; Olsson and Brown, 1993; Brown, 1995; Matsuki et al., 2006; Candela et al., 2012; Ishibashi et al., 2015; Sawayama et al., 2021a, 2021b). Data in (c) from: (Sharifzadeh et al., 2008; Watanabe et al., 2008, 2009; Nemoto et al., 2009; Ishibashi et al., 2015; Fathi et al., 2016; Wenning et al., 2019). The contact area ranges in Table 1 are the 25th-75th percentile in (c), i.e. the extent of the boxes for measurements at $\geq$20 MPa.

4. Results

4.1. Properties of individual faults

4.1.1. Permeability

Fault permeability distributions, and fault resistivity distributions from three of the modelled fluid resistivities are shown in Fig. 4. For faults with no displacement, permeability in both directions has a strong peak at ~5 × 10^{-14} m^2. For faults with 1 mm displacement, permeability perpendicular to slip peaks at a lower permeability (2 × 10^{-14} m^2), while fault permeability parallel to slip peaks higher (9 × 10^{-14} m^2).

For faults with 2–3 mm displacement, peak permeability is similar to those with 0–1 mm displacement, but the distributions have long positive tails. For faults with displacement ≥5 mm, the peak in permeability

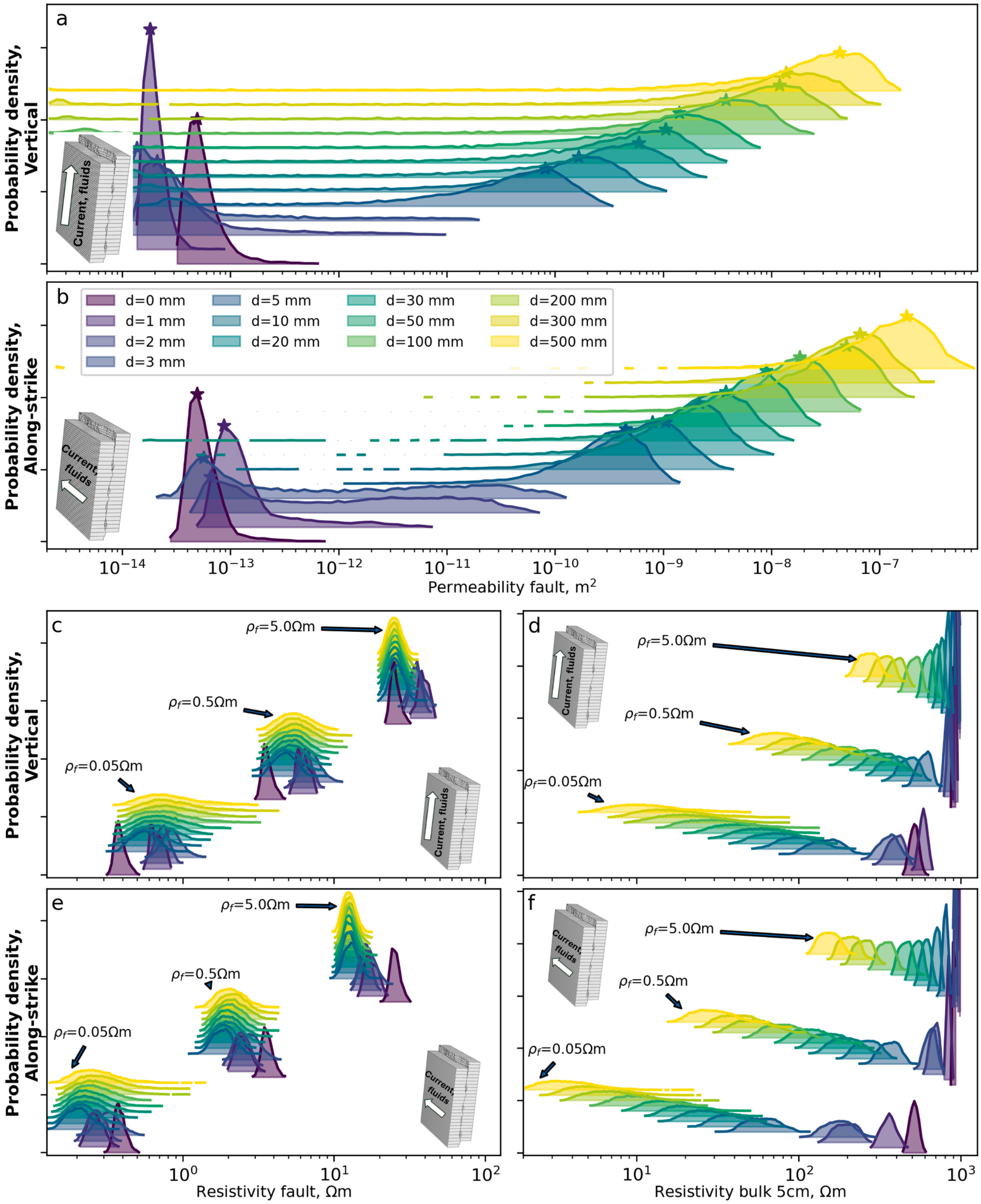

Fig. 4. Resistivity and permeability of individual faults from modelling displayed as smoothed histograms, coloured by fault displacement. Histograms are displacement vertically to aid visualisation. (a) and (b): Fault permeability, modelled parallel ("vertical") and perpendicular ("along-strike") to slip direction. (c) and (e): Fault resistivity, modelled parallel ("vertical") and perpendicular ("along-strike") to slip direction. (d) and (f): resistivity of a 5 cm wide model cell containing a fault with displacement D, i.e. these resistivity values form the inputs to the upscaled models. Panels (c) to (f) show resistivity values for faults containing a material with three resistivities (ρ_f), as labelled on the figure, i.e. 0.05 Ωm, 0.5 Ωm, and 5.0 Ωm. The stars denote the peak of permeability used to calculate the roughness factor beta (Equation 5; Section S6).

increases with displacement for vertical and along-strike directions (Fig. 4). This likely reflects larger aperture in these models. The permeability at the peak can be predicted reasonably well by a global parallel plate model using the mean aperture *b* and roughness factor β, a multiplier to the physical aperture (Kissling and Massiot, 2023), i.e.

$$k_{peak} = \frac{(\beta b)^2}{12} \tag{5}$$

Where $\beta \approx 0.404$ in the direction perpendicular to slip. The mean aperture *b* in mm can be predicted from displacement, *d*, to within 1% (for displacement ≥ 5 mm) by the expression:

$$b = 0.056\ d^{0.668} \tag{6}$$

In models parallel to the slip direction, a roughness factor β of 0.190 in Eq. (5) can be used to predict the position of the main peak. Fitting of Eqs. (5) and (6) is described in Section S5. In these models, there is also a small peak at $<\sim 1 \times 10^{-13}$ m^2 that decreases with displacement, suggesting a small proportion of these faults are below their percolation threshold.

4.1.2. *Resistivity*

Fault resistivities show a more compact distribution than permeability, and little variation in resistivity with varying length or displacement. This demonstrates that the roughness effect on resistivity does not change substantially with displacement. However, the averaged resistivity over a constant width (i.e. the resistivity used in the

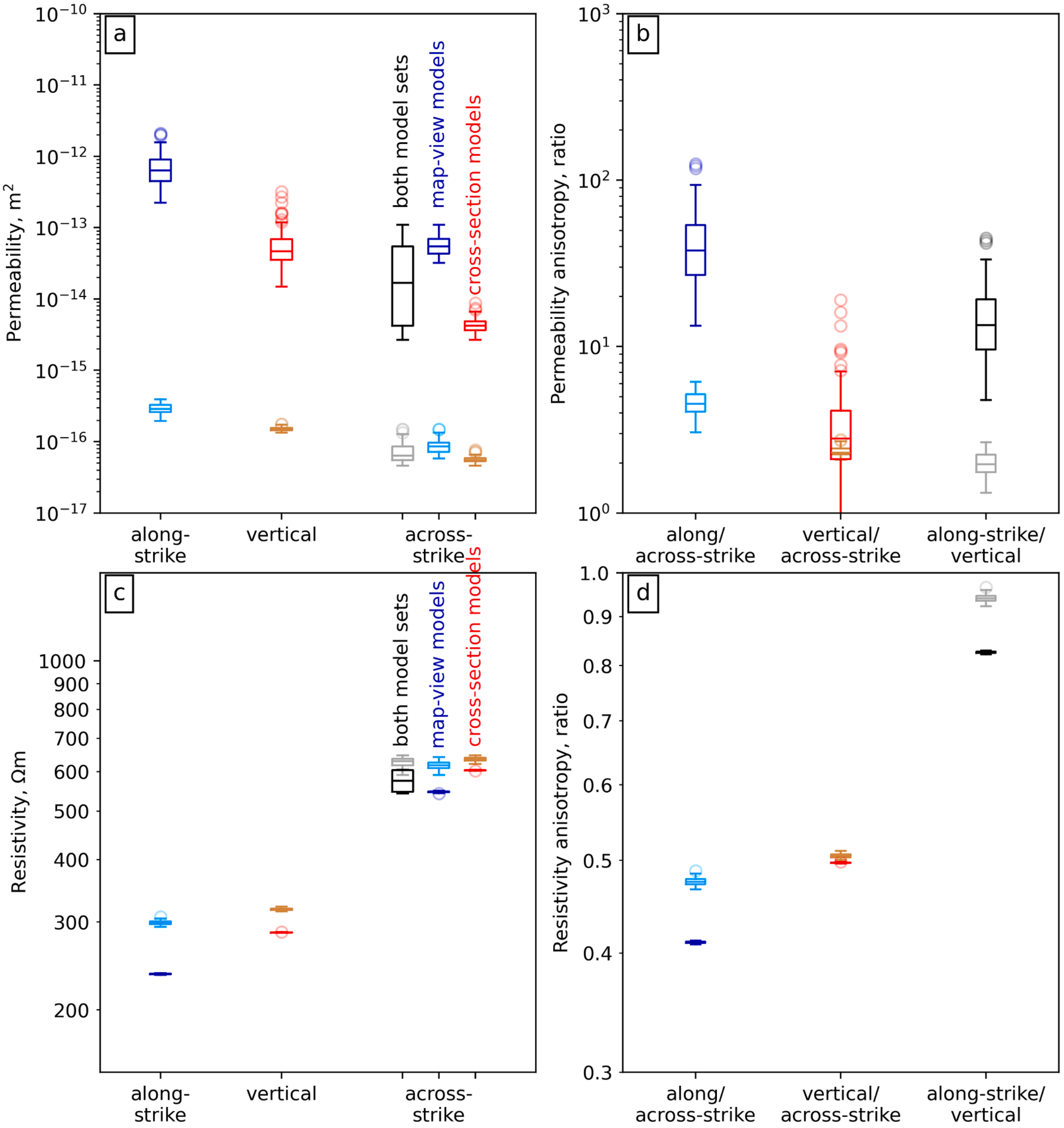

Fig. 5. Permeability and resistivity of a faulted reservoir from modelling shown as box and whisker plots. (a) along-strike, vertical, and across-strike permeability in a normal faulting (TVZ-type) regime, with across-strike given as both individual plots for the map-view and cross-section view models, as well as a single box and whisker for all across-strike models combined, (b) along/across-strike, vertical/across-strike, and along-strike/vertical permeability anisotropy ratios, using the median across both across-strike models. (c) and (d) show equivalents to (a) and (b) for resistivity. Light coloured boxes represent 'micro-fault' permeability determined by modelling an 0.5 × 0.5 m area containing faults ≤0.2 m in size. Darker boxes represent 'macro-scale' permeability determined by modelling a 80 × 80 m area. Boxes show the 25th and 75th percentile with line at the median (computed in log space), fliers are shown semi-transparent to aid visualisation of clusters of points.

reservoir-scale models) decreases with fault displacement, reflecting the increased average aperture associated with larger displacement.

The width of the resistivity histograms is wider (in log-space) for faults filled with lower resistivity fluid, compared to those with higher resistivity fluid, reflecting the larger contrast in resistivity between the rock and the fluid. Resistivity of faults in the direction parallel to displacement is higher than resistivity perpendicular to slip, by a factor of 2 ($\rho_f = 5$ Ωm) to 3 ($\rho_f = 0.05$ Ωm).

4.2. *Properties of a faulted volume*

Permeability and resistivity of a faulted volume (base case scenario) are shown in Fig. 5. Parameter variations are shown in the following four plots; variation with the proportion of along-strike or vertical faults P_z (Fig. 6), variation with the fault density exponent γ (Fig. 7), and variation with the fluid resistivity ρ_f (Fig. 9). “Map-view” and “cross-section view” terms refer to Fig. 1.

4.2.1. *Base case*

Reservoir-scale permeability is highest along-strike (6×10^{-13} m^2). Vertical reservoir-scale permeability is intermediate in magnitude (5×10^{-14} m^2). The across-strike permeability is about an order of magnitude higher for the “map-view” than the “cross-section view” models i.e., 5×10^{-14} m^2 versus 4×10^{-15} m^2, with the median (in log-space) equal to 2×10^{-14} i.e. slightly lower than vertical permeability. The contribution of micro-faults to the overall permeability is low in all cases ($<3 \times 10^{-16}$ m^2). Permeability anisotropy is ~40 (along/across-strike), and 3 (vertical/across-strike), however there is significant uncertainty around these numbers (visualised by shaded ranges in Fig. 6) due to uncertainty in the across-strike permeability.

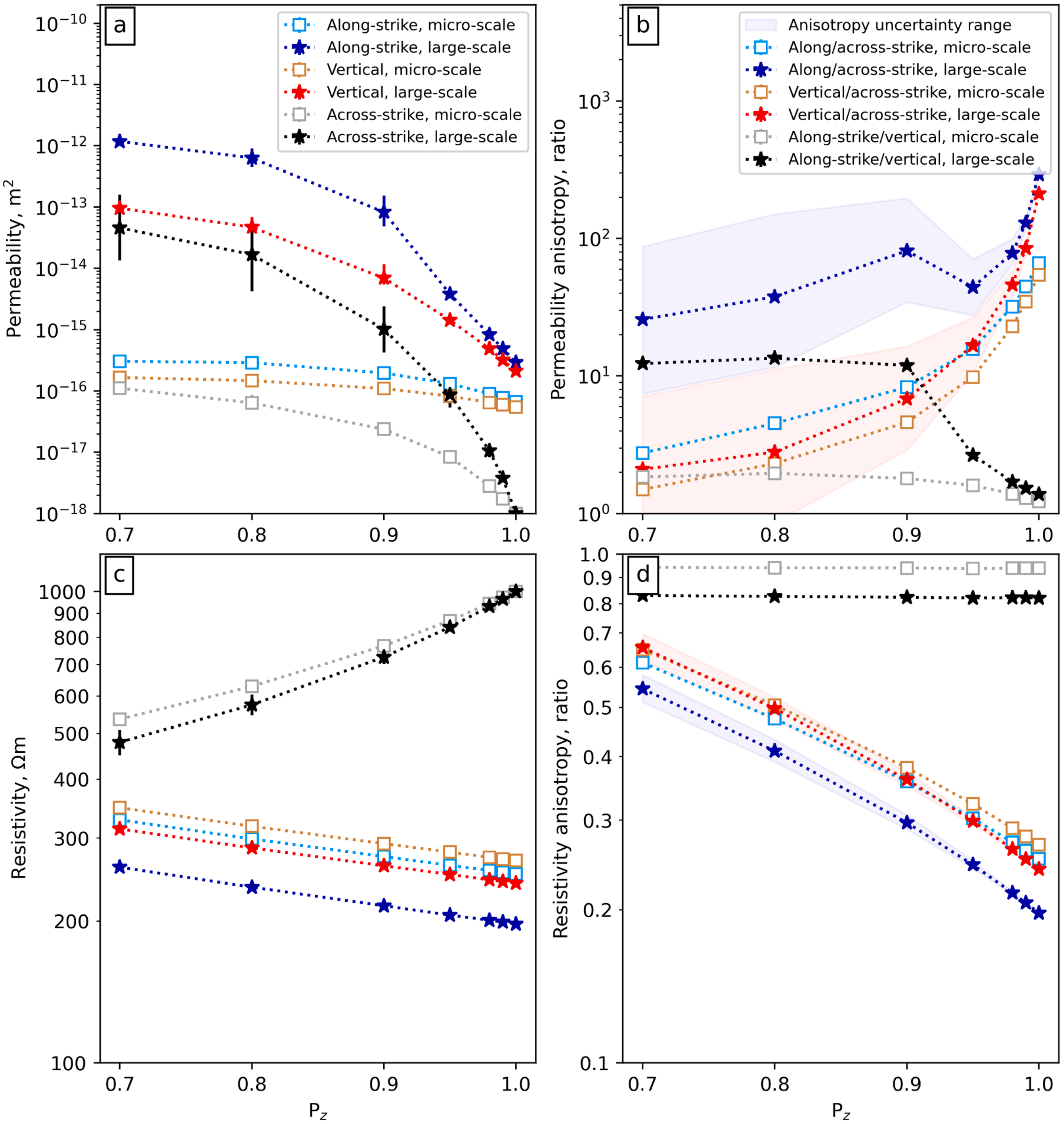

Fig. 6. Permeability and resistivity as a function of the proportion of faults along the dominant strike direction (Pz). (a) permeability in three directions (b) corresponding permeability anisotropy ratios, (c) resistivity in three directions, and (d) corresponding resistivity anisotropy ratios. (a) and (c) are shown as error bar plots with the errorbars representing the inter-quartile range, (b) and (d) are shown as points with error ranges shaded in the along-strike and vertical cases representing the range due to using either of the two different across-strike results to compute the anisotropy ratio as opposed to the median of both (symbols and dotted lines).

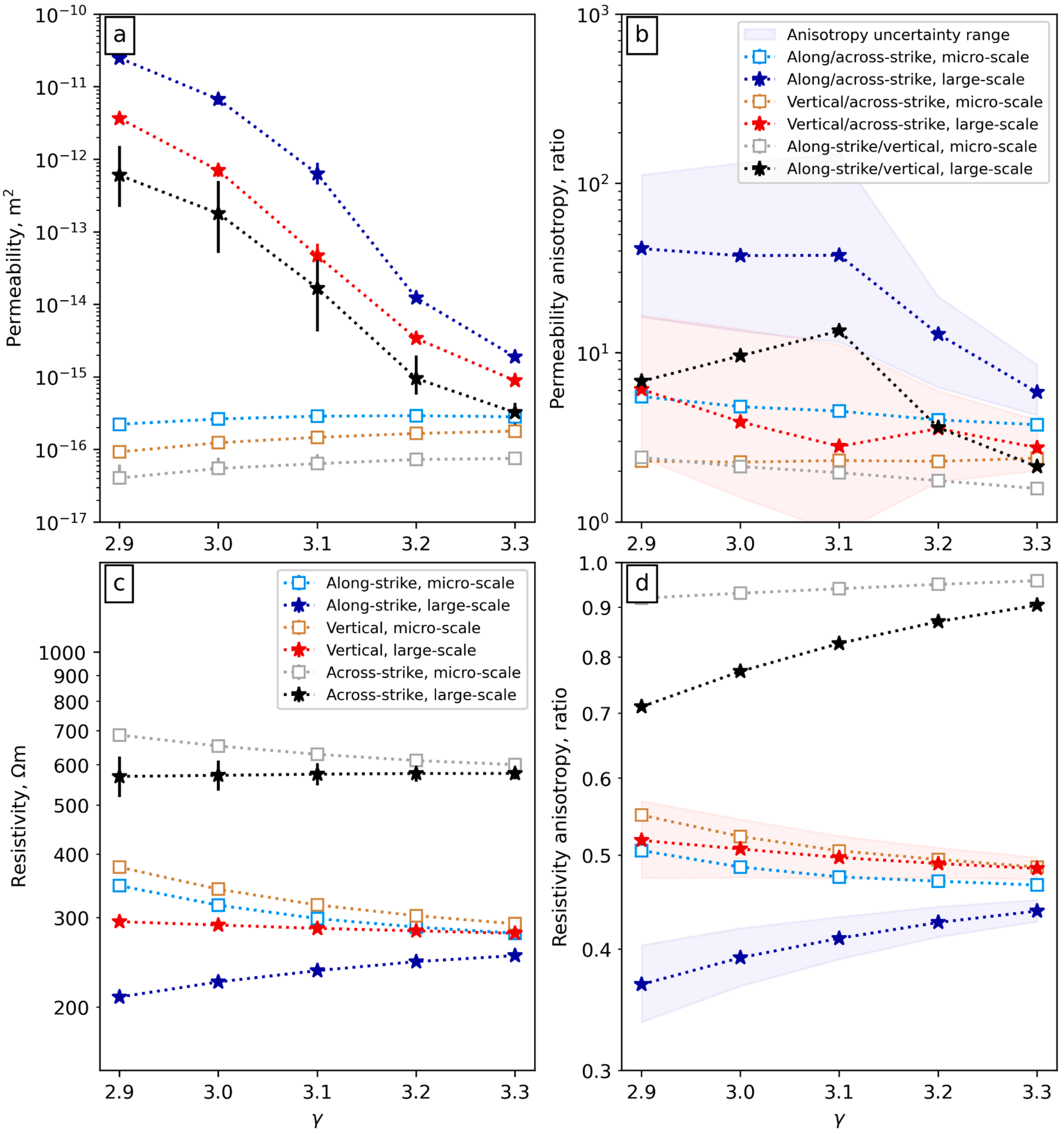

Fig. 7. Permeability and resistivity as a function of the fault density exponent γ. (a) permeability in three directions (b) corresponding permeability anisotropy ratios, (c) resistivity in three directions, and (d) corresponding resistivity anisotropy ratios. (a) and (c) are shown as error bar plots with the errorbars representing the interquartile range, (b) and (d) are shown as points with error ranges shaded in the along-strike and vertical cases representing the range due to using either of the two different across-strike results to compute the anisotropy ratio as opposed to the median of both (symbols and dotted lines).

Along-strike and vertical resistivity are similar, 235 and 285 Ωm respectively, while across-strike resistivity is well-constrained (compared to permeability) at 575 (±30) Ωm. Correspondingly, along-strike/vertical resistivity ratio is close to 1 (0.8) while along/across-strike and vertical/across-strike resistivity anisotropy ratios are around 0.38 and 0.5 respectively. Micro-scale resistivity anisotropy is almost the same as reservoir-scale, i.e. most of the inferred anisotropy is due to micro-scale faults.

4.2.2. *Influence of P_z*

The proportion of along-strike faults, P_z, has a moderate impact on permeability in the range 0.7 to 0.9, with along-strike and vertical permeability decreasing by a factor of five over this range. Across-strike permeability decreases by slightly more over this range, so anisotropy ratio increases. Between $P_z = 0.9$ and 1.0, along-strike and vertical permeability drops nearly to micro-fault level ($<1 \times 10^{-15}$), and across-strike permeability drops to matrix values. Therefore, at least 10% of cross-faults are needed to provide a fully connected network.

Along/across-strike resistivity anisotropy ratio decreases with P_z, to a minimum of 0.2 for P_z=1.0. The increase in anisotropy ratio is mainly due to an increase in across-strike resistivity, as the along-strike resistivity only decreases by 25% over the tested P_z range (Fig. 6).

4.2.3. *Influence of fault density exponent*

The value of the exponent γ, which controls the relative numbers of long vs short faults, strongly controls reservoir-scale permeability, but has only a small impact on micro-fracture permeability (Fig. 7). An increase of γ from 2.9 to 3.3 (i.e., progressively reducing the relative number of long faults) decreases reservoir-scale permeability by about four orders of magnitude. On the other hand, micro-scale permeability barely changes over this range. This suggests that the large faults have a greater effect on permeability than the more numerous smaller faults.

In contrast, γ has a minor influence on resistivity and resistivity anisotropy. Along-strike resistivity increases by 21% over the tested range, while both vertical and along-strike resistivity change by <6%. Accordingly, there is a small change in along/across-strike resistivity ratio over this γ range (0.37 to 0.44).

4.2.4. *Influence of porosity*

Both micro-fracture and reservoir-scale permeability increases with fracture porosity as may be expected, however this is non-linear, likely because the 1%-porosity fault volumes are below their fluid-flow percolation threshold. A porosity increase from 1 to 1.5% results in permeability increasing by two orders of magnitude, while an increase from 1.5 to 2% increases permeability by a factor of 3–5 (Fig. 8).

Porosity is the strongest control on resistivity, with a change from 1 to 2% decreasing along-strike resistivity by a factor of 2.5. Along/across-strike resistivity ratio changes from 0.48 to 0.35 over this porosity range.

4.2.5. *Influence of fluid resistivity*

Median bulk resistivity anisotropy follows a near-sigmoidal relationship as a function of the ratio of matrix to fluid resistivity ρ_m/ρ_f (in log-log space), increasing again at very low fluid resistivities (Fig. 9). This means that very low fluid resistivities by themselves do not increase the anisotropy ratio of a reservoir much beyond a factor of around 3. However, a combination of very low proportion of faults across the dominant strike, with low fluid resistivities, may increase the anisotropy ratio higher than in the presented models.

5. Discussion

5.1. *Comparison to field measurements and other models*

Field measurements and models developed with other approaches provide a means to assess the validity of the numerical model results,

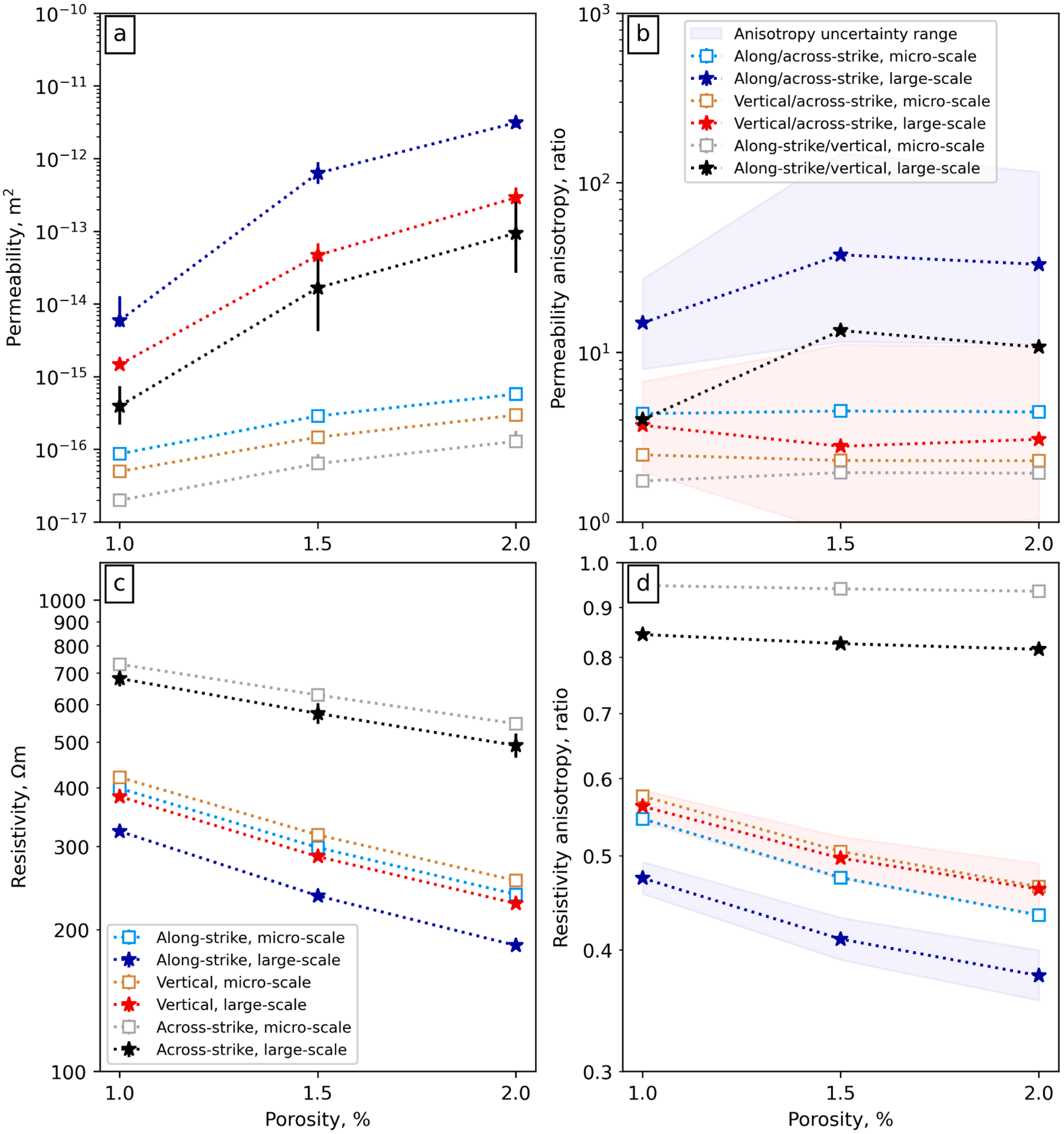

Fig. 8. Permeability and resistivity as a function of fracture porosity. (a) permeability in three directions (b) corresponding permeability anisotropy ratios, (c) resistivity in three directions, and (d) corresponding resistivity anisotropy ratios. (a) and (c) are shown as error bar plots with the errorbars representing the interquartile range, (b) and (d) are shown as points with error ranges shaded in the along-strike and vertical cases representing the range due to using either of the two different across-strike results to compute the anisotropy ratio as opposed to the median of both (symbols and dotted lines).

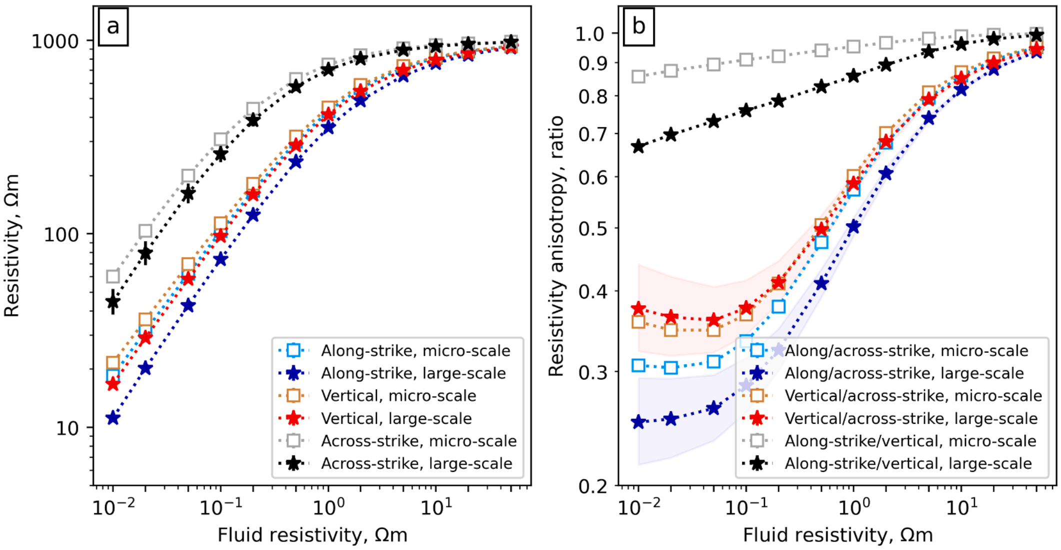

Fig. 9. Resistivity as a function of fluid resistivity. (a) resistivity in three directions, and (b) corresponding resistivity anisotropy ratios. (a) shown as error bar plots with the errorbars representing the inter-quartile range, (b) is shown as points with error ranges shaded in the along-strike and vertical cases representing the range due to using either of the two different across-strike results to compute the anisotropy ratio as opposed to the median of both (symbols and dotted lines).

since, to our knowledge, no similar approach of modelling resistivity and permeability through fault networks exist. For permeability, reservoir models calibrated to reservoir pressure and temperature histories provide a ground-truth. For resistivity, ground-truthing data includes borehole resistivity logs and geophysical data.

5.1.1. *Permeability*

Bulk vertical permeability in geothermal reservoir models ranges from around 10^{-15} to 10^{-13} m^2 in TVZ fields (Dempsey et al., 2011; Baars et al., 2023; van Driel et al., 2023; Rajput et al., 2024). Permeability is unlikely to be much higher than this on a large scale as it is difficult to maintain stable convection (Scott et al., 2016; Pearson-Grant and Bertrand, 2021). Fault models presented here have vertical and across-strike permeabilities consistent with those of isotropic permeability in reservoir models (Fig. 5a). The along-strike permeabilities in our models are about an order of magnitude higher than values associated with stable convection. However, in reservoir models, the highest pressure gradients are likely vertical due to the competition between buoyancy and gravitational forces. If there is only a weak pressure gradient along-strike, then there may be little sensitivity in the models to along-strike permeability, in which case along-strike permeabilities could be realistic.

Discrete fracture network-derived permeability model based on a TVZ-like setting presented by Kissling and Massiot (2023) used a different approach to our method and offers a useful comparison. Those models were 2D, in “cross-section” view. Fractures were modelled as sticks with a constant length to aperture ratio but had a range of fracture dip magnitudes rather than constraining fault orientation to two orthogonal directions. The β factor, which relates geometric to hydraulic aperture, is different in Kissling and Massiot (2023) (β=0.002) to our models (β=0.185), but this is because their geometric aperture represents the total width of the fracture, different from our mean aperture. Additionally, we find that the fault length-aperture relationship is a power law with exponent <1 (Eq. (6)), i.e., larger fractures have smaller apertures relative to length than smaller fractures. Consequently, their models have less permeable faults than us, but with higher fracture porosity. Overall, modelled reservoir-scale vertical permeabilities of Kissling and Massiot (2023) are very similar to our models (3×10^{-14} to 1.3×10^{-13} m^2, vs 5×10^{-14} in this paper). If we consider the across-strike result from our “cross-section” models (Fig. 5), then the across-strike permeabilities and horizontal/vertical permeability anisotropy ratio (~13) are also very similar to our models.

Conversely, permeability of individual faults measured in the lab (Watanabe et al., 2008, 2009; Ishibashi et al., 2015) generally report permeabilities higher than from our models, e.g. for faults with no displacement, measured permeabilities are around 10^{-12} to 10^{-11} m^2, compared to 10^{-13} to 10^{-12} m^2 in our models. For faults with 5 mm displacement, measured permeabilities of 10^{-9} to 10^{-8} m^2 are about an order of magnitude higher than our models. However, this difference can be explained by the fact that induced faults generally have higher roughness amplitude (scaling factor) than natural faults (Fig. 3) and scaling factor has a strong effect on permeability. A numerical modelling study of resistivity and permeability of individual fractures using a similar approach to this study demonstrated this sensitivity, showing that, for example, halving scaling factor reduces permeability by an order of magnitude (Sawayama et al., 2023). The Sawayama et al. (2023) study modelled fractures with small offsets (0.0 to 1.5 mm) at variable normal stress, and overall, the permeability ranges (10^{-13} to 10^{-11} m^2 for faults with no displacement; 10^{-12} to 10^{-9} m^2 for 1.5 mm displacement) overlap with our models, although there is high sensitivity to the input parameters chosen.

5.1.2. *Resistivity*

In geothermal wells, downhole resistivity measurements are rarer than surface geophysical techniques and only penetrate up to ~1 m into the formation. However, they provide greater certainty on absolute resistivity. At the Ngā Tamariki geothermal field, New Zealand, reservoir resistivity was measured at 30 – 100 Ωm, lower than our models. This may reflect a lower host rock resistivity – which was primarily tuff and volcaniclastic rocks.

The primary surface geophysical technique used to measure resistivity in geothermal reservoirs is MT as it is normally the only method with enough depth penetration to image reservoirs at >2 km depth. Absolute resistivity variations from MT inversion are sensitive to the prior model (Robertson et al., 2020), compounded by reduced sensitivity below the conductive clay cap in geothermal systems. However, resistivities of 200 to 300 Ωm, which we predict for reservoirs containing 0.5 Ωm fluid and 1000 Ωm rock matrix, are consistent with resistivity in the reservoir zone in MT inversions of TVZ geothermal systems (e.g., Heise et al., 2008, 2016; Bertrand et al., 2013, 2022).

There are few conclusive measurements of resistivity anisotropy measured from the surface, and there is likely high uncertainty in anisotropy ratios due to the ambiguity between anisotropy and 2D/3D structure. An experiment designed to measure resistivity anisotropy using controlled-source electromagnetic (EM) data over the East Pacific Rise found resistivity along-strike of the mid ocean ridge approximately 18–36 times lower than perpendicular to it, interpreted as sub-vertical fault zones (Chesley et al., 2019). These ratios are higher than determined from our models. Being in saltwater, fluid resistivities beneath the East Pacific Rise may be lower than our modelled fluid resistivities and this combined with a higher proportion of along-strike faults may produce anisotropy ratios encompassing the measured range. Alternatively the inconsistency may reflect uncertainty in the EM inversions; geophysical inversions are non-unique, and EM inversions can overestimate extreme values; the 70 and 90th percentile scenarios reported by Chesley et al. (2019) encompassed scenarios with anisotropy ratios as low as a factor of about 3, consistent with our results (Fig. 9).

At the other end of the fluid resistivity scale, resistivity anisotropy was measured using the DC resistivity method for understanding fractured aquifers (Lane et al., 1995; Odoh and Onwuemesi, 2009; George et al., 2010; Yeboah-Forson and Whitman, 2014; Ani et al., 2023). Water resistivity is only reported in one of these studies (14 Ωm), however we assume that groundwater intended as drinking/irrigation supply is likely to have a relatively high resistivity, >10 Ωm based on an assumption of <250 ppm NaCl from World Health Organization guidelines (World Health Organisation, 2023) and <30 °C (Light et al., 2005). Reported anisotropy ratios in these studies of around 1.01 to 1.4 are consistent with our models for fluid resistivity >10 Ωm.

5.2. Implications for fractured reservoir permeability characterisation

In this section, we discuss how modelled permeability and resistivity values provide constraints that are helpful in (1) developing realistic reservoir models, (2) interpreting resistivity anomalies from surface-based geophysical techniques such as MT, and (3) linking fault density parameters determined from boreholes to permeability and resistivity. The discussion generally applies to fractured reservoirs, though especially in geothermal reservoirs where MT surveys are commonly conducted to map the heat source and clay cap.

Modelling predicts that the fault permeability perpendicular to slip is about seven times higher than that parallel. In an extensional regime like the TVZ, this would mean that vertical permeability is lower than horizontal along-strike permeability. This result numerically demonstrates the qualitative prediction that fault irregularities should enhance permeability most strongly along the direction perpendicular to slip (Sibson, 2000; Rowland and Simmons, 2012). Analogous to permeability, fault resistivity perpendicular to fault slip is lower than that parallel to slip, though by a smaller factor of 2–3 (Fig. 4).

In general, resistivity shows much lower sensitivity to fault length distribution and porosity than permeability. Therefore, there are many permeability scenarios consistent with a given resistivity. Consequently, resistivity-based techniques alone are unlikely to be able to uniquely map permeability in a reservoir. However, there are some aspects of the resistivity tensor that may be useful in understanding permeability distribution within a reservoir and particularly directional dependence of permeability.

Since across-strike resistivity is uniformly higher than along-strike resistivity, then if the host rock is isotropic and fractures are fluid filled, measuring the resistivity tensor should resolve the orientation of the most permeable structures. In MT, and other surface-based resistivity surveying techniques, resistivity differences of 235 Ωm (along-strike) versus 575 Ωm (across-strike) may be resolvable near the surface, as shown in groundwater studies (Section 5.1.2). However, beneath a conductive clay surface layer with resistivity ~3 Ωm these resistivities are likely to be a subtle signal, difficult to uniquely resolve. A potential avenue of future work could be to examine the potential for utilising borehole to borehole measurements to measure resistivity within a reservoir, including the possibility of using steel boreholes as long electrodes (Rucker et al., 2011; Zhang et al., 2014; Heagy and Oldenburg, 2019), which would avoid signal needing to penetrate a conductive surface layer. Additionally, well logging tools to determine directional resistivity are applied in the petroleum industry (Leveridge, 2010; Horstmann et al., 2015; Wang et al., 2020). If such tools could be developed to handle geothermal conditions, they may be a useful tool for understanding the resistivity, and hence permeability, tensor in a geothermal reservoir.

Along-strike, vertical and across strike resistivity are nearly equally sensitive to porosity, so resistivity anisotropy ratio is not highly sensitive to porosity. Since resistivity is also sensitive to matrix resistivity (controlled by lithology, alteration, temperature etc.), it would be necessary to accurately characterise matrix resistivity (e.g. using core measurements) before absolute resistivity could be used as a proxy for porosity.

Across-strike resistivity (and consequently, resistivity anisotropy) is most sensitive to the proportion of along-strike faults, or P_z. If we assume that matrix resistivity is isotropic, then resistivity anisotropy *may* be useful in mapping relative proportions of faults along different directions, and thus targeting permeable zones within a reservoir.

5.3. Model limitations and next steps

This work represents an important next step in linking electrical resistivity and permeability at the core to field scale. However, the approach has several limitations that could be addressed in future work.

Firstly, the models are 2D, so full resistivity and permeability tensors are not captured. Implementing the approach in 3D would capture the effects of interactions between differently oriented faults in three directions, and fault intersections. Secondly, the modelling is carried out on orthogonal axes, rather than using the true geometry of faults, which show a range of orientations. Allowing arbitrary orientations would make the models more realistic.

Thirdly, the maximum model size is 80 × 80 m, which is similar in scale to a single cell in reservoir models (Baars et al., 2023; O'Sullivan et al., 2025). Upscaling the models further requires careful consideration of damage zones and gouge or rock fragments in faults. These are likely to result in permeabilities that are lower than what we have modelled due to reduced aperture sizes compared to a single fault with no damage, unless compensated by increased density of secondary faults in the damage zone (Faulkner et al., 2010).

The fractures are assumed to contain only fluids, and of course, if some of the fractures are mineralised or filled with clay, they may be conductive but not permeable and have effects on resistivity that are not expressed in permeability. These effects, which also hinder borehole image interpretation, could be understood further through measurements on core and outcrop to identify the characteristics and extent of conductive but not permeable zones. Joint inversion of seismic anisotropy and resistivity may have the potential to remove some of this ambiguity and help to image permeable fracture zones.

Finally, both fluid and current are modelled using simplified models, although these are likely to be adequate given other uncertainties in the modelling. Permeability and resistivity are modelled using, respectively, the modified local parallel plate model, and Ohm's Law, excluding any surface conductance or frequency dependent effects. The local parallel plate model is likely to be a reasonable approximation given the high sensitivity of the permeability calculations to inputs, i.e. changes in porosity, γ and P_z result in orders of magnitude changes in permeability. Thus errors due to mis-characterisation of model inputs are likely to dominate over inaccuracies in the parallel plate model which are estimated to be $<10\%$ for low flow rates (Brush and Thomson, 2003). Neglecting surface conductance and frequency-dependent conductivity are likely to have minimal effect on the overall conductivity, with data suggesting small effects relative to the bulk electrolyte conductivity, with a smaller relative effect at high salinities and temperatures (Revil and Glover, 1998). However, surface conductivity effects in very high temperatures (e.g. supercritical) are unknown and could potentially be significant.

6. Conclusions

Two-dimensional numerical modelling of a faulted reservoir has estimated, for the first time, direction-dependent permeability and resistivity at reservoir scale (80 × 80 m), linking resistivity with permeability, and linking the core to the reservoir scale. Permeability is highest in the horizontal along-dominant-strike direction, lower vertically, and lowest in the horizontal across-dominant strike direction. Resistivity is lowest along the dominant strike, slightly higher in the vertical direction and highest across-strike. While these differences in resistivity with orientation are likely detectable if present at the surface, it may be challenging to resolve these beneath a conductive clay cap of a geothermal field.

Resistivity has low sensitivity to fracture length distribution, with all resistivity predictions for a given direction within a factor of 2–3. Resistivity shows highest sensitivity to fracture porosity and the proportion of along-strike faults. Permeability shows strong sensitivity to fracture length distribution and porosity. There is a permeability range of about four orders of magnitude across the different parameter combinations.

Resistivity anisotropy is one of the least sensitive parameters to model inputs, remaining relatively constant for different fault network parameters. It shows strongest sensitivity to the proportion of faults along the dominant strike direction (P_z). Conversely, permeability along the dominant strike of the fault zone is not highly sensitive to P_z, except at very high P_z values where the lack of across-strike faults inhibits a full fault network connection.

Acknowledgments

The authors would like to thank Warwick Kissling for useful discussions and for reviewing an earlier version of this paper, as well as four anonymous reviewers. This project was supported by the New Zealand Ministry of Business, Innovation and Employment (MBIE) through the Energy Futures programme (Strategic Science Investment Fund, contract C05X1702).

CRediT authorship contribution statement

Alison Kirkby: Writing – review & editing, Writing – original draft, Visualization, Validation, Software, Methodology, Investigation, Formal analysis, Data curation, Conceptualization. **Cécile Massiot:** Writing – review & editing, Validation, Methodology, Data curation.

Declaration of competing interest

The authors declare the following financial interests/personal relationships which may be considered as potential competing interests: Alison Kirkby reports financial support was provided by Ministry of Business Innovation and Employment. If there are other authors, they declare that they have no known competing financial interests or personal relationships that could have appeared to influence the work reported in this paper.

Supplementary materials

Supplementary material associated with this article can be found, in the online version, at doi:10.1016/j.geothermics.2026.103620.

Data availability

The code used for these models is available at https://github.com/alkirkby/resistor_network. Final model results, and a copy of the code version as used in this article, are available from https://doi.org/10.5281/zenodo.18307615 (Kirkby 2026).

References

Ani, C.C., Akpa, C., Obasi, P.N., Chukwu, A., 2023. Integrated electrical resistivity methods for evaluation of fracture terrain groundwater potentials, case study of indurated shale of Lower Benue trough, Southeastern Nigeria. Groundw. Sustain. Dev. 23, 101014.

Ardid, A., Dempsey, D., Bertrand, E., Sepulveda, F., Tarits, P., Solon, F., Archer, R., 2021. Bayesian magnetotelluric inversion using methylene blue structural priors for imaging shallow conductors in geothermal fields. Geophysics 86 (3), E171–E183.

Baars, M., Renaud, T., Riffault, J., O'Sullivan, M.J., O'Sullivan, J., Gravatt, M., Dekkers, K., Speetjens, M., 2023. Numerical model of the Tikitere geothermal system. In: Proceedings of the 45th New Zealand Geothermal Workshop. Auckland, New Zealand.

Bahr, K., 1997. Electrical anisotropy and conductivity distribution functions of fractal random networks and of the crust: the scale effect of connectivity. Geophys. J. Int. 130 (3), 649–660.

Bannard, J.E., 1975. Effect of density on the electrical conductance of aqueous sodium chloride solutions. J. Appl. Electrochem. 5 (1), 43–53.

Bertrand, E.A., Caldwell, T.G., Bannister, S., Soengkono, S., Bennie, S.L., Hill, G.J., Heise, W., 2015. Using array MT data to image the crustal resistivity structure of the southeastern Taupo Volcanic Zone, New Zealand. J. Volcanol. Geotherm. Res. 305, 63–75.

Bertrand, E.A., Caldwell, T.G., Hill, G.J., Bennie, S.L., Soengkono, S., 2013. Magnetotelluric imaging of the Ohaaki geothermal system, New Zealand: implications for locating basement permeability. J. Volcanol. Geotherm. Res. 268, 36–45.

Bertrand, E.A., Kannberg, P., Caldwell, T.G., Heise, W., Constable, S., Scott, B., Bannister, S., Kilgour, G., Bennie, S.L., Hart, R., Palmer, N., 2022. Inferring the magmatic roots of volcano-geothermal systems in the Rotorua Caldera and Okataina Volcanic Centre from magnetotelluric models. J. Volcanol. Geotherm. Res. 431, 107645.

Bibby, H.M., Caldwell, T.G., Davey, F.J., Webb, T.H., 1995. Geophysical evidence on the structure of the Taupo Volcanic Zone and its hydrothermal circulation. J. Volcanol. Geotherm. Res. 68 (1), 29–58.

Bolós, X., Cifuentes, G., Macías, J.L., Sosa-Ceballos, G., Garcia-Tenorio, F., Albor, M., 2019. Geophysical imaging of fluid circulation and its relation with the structural system of Cerritos Colorados geothermal field, La Primavera caldera (Mexico). J. Volcanol. Geotherm. Res. 369, 238–249.

Bonnet, E., Bour, O., Odling, N.E., Davy, P., Main, I., Cowie, P., Berkowitz, B., 2001. Scaling of fracture systems in geological media. Rev. Geophys. 39 (3), 347–383.

Brown, S.R., 1989. Transport of fluid and electric current through a single fracture. J. Geophys. Res. Solid Earth 94 (B7), 9429–9438.

Brown, S.R., 1995. Simple mathematical model of a rough fracture. J. Geophys. Res. Solid Earth 100 (B4), 5941–5952.

Brown, S.R., Scholz, C.H., 1986. closure of rock joints. J. Geophys. Res. Solid Earth 91 (B5), 4939–4948.

Browne, P.R.L., 1970. Hydrothermal alteration as an aid in investigating geothermal fields. Geothermics 2, 564–570.

Brush, D.J., Thomson, N.R., 2003. Fluid flow in synthetic rough-walled fractures: navier-stokes, stokes, and local cubic law simulations. Water Resour. Res. 39 (4), 5-1–5-15.

Calibugan, A., Melia, K., Rivera, M., 2022. Conceptual model update for the Rotokawa geothermal field, New Zealand. In: Proceedings of the 44th New Zealand Geothermal Workshop. Auckland, New Zealand, p. 8.

Candela, T., Renard, F., Klinger, Y., Mair, K., Schmittbuhl, J., Brodsky, E.E., 2012. Roughness of fault surfaces over nine decades of length scales. J. Geophys. Res. Solid Earth 117 (B8), 1–30.

Cant, J.L., Siratovich, P.A., Cole, J.W., Villeneuve, M.C., Kennedy, B.M., 2018. Matrix permeability of reservoir rocks, Ngatamariki geothermal field, Taupo Volcanic Zone, New Zealand. Geotherm. Energy 6 (1), 2.

Chambefort, I., Buscarlet, E., Wallis, I.C., Sewell, S., Wilmarth, M., 2016. Ngatamariki Geothermal Field, New Zealand: geology, geophysics, chemistry and conceptual model. Geothermics 59, 266–280.

Chambefort, I., Lewis, B., Wilson, C.J.N., Rae, A.J., Coutts, C., Bignall, G., Ireland, T.R., 2014. Stratigraphy and structure of the Ngatamariki geothermal system from new zircon U–Pb geochronology: implications for Taupo Volcanic Zone evolution. J. Volcanol. Geotherm. Res. 274, 51–70.

Chen, G., Spetzler, H., 1993. Topographic characteristics of laboratory induced shear fractures. Pure Appl. Geophys. 140 (1), 123–135.

Chesley, C., Key, K., Constable, S., Behrens, J., MacGregor, L., 2019. Crustal cracks and frozen flow in oceanic lithosphere inferred from electrical anisotropy. Geochem. Geophys. Geosyst. 20 (12), 5979–5999.

Dempsey, D., Rowland, J.V., Archer, R., Ellis, S., 2011. Modelling geothermal circulation in a "TVZ-like" setting. In: Proceedings of the New Zealand Geothermal Workshop. Auckland, New Zealand.

Dezayes, C., Albert, G., Benoît, V., 2010. Structure of the low permeable naturally fractured geothermal reservoir at Soultz. Comptes Rendus. Géosci. 342 (7–8), 517–530.

Fathi, A., Moradian, Z., Rivard, P., Ballivy, G., Boyd, A.J., 2016. Geometric effect of asperities on shear mechanism of rock joints. Rock. Mech. Rock. Eng. 49 (3), 801–820.

Faulkner, D.R., Jackson, C.A.L., Lunn, R.J., Schlische, R.W., Shipton, Z.K., Wibberley, C. A.J., Withjack, M.O., 2010. A review of recent developments concerning the structure, mechanics and fluid flow properties of fault zones. J. Struct. Geol. 32 (11), 1557–1575.

Franzson, H., Zierenberg, R., Schiffman, P., 2008. Chemical transport in geothermal systems in Iceland: evidence from hydrothermal alteration. J. Volcanol. Geotherm. Res. 173 (3), 217–229.

George, A.M., Okiwelu, A.A., Obi, D.A., 2010. DC-resistivity estimation of second porosity and anisotropy using azimuthal resistivity surveys: a case study of part of Oban Massif and Obudu Plateau, southeastern, Nigeria. Res. J. Earth Sci. 2 (2), 24–29.

Heagy, L.J., Oldenburg, D.W., 2019. Modeling electromagnetics on cylindrical meshes with applications to steel-cased wells. Comput. Geosci. 125, 115–130.

Heap, M.J., Kennedy, B.M., 2016. Exploring the scale-dependent permeability of fractured andesite. Earth Planet. Sci. Lett. 447, 139–150.

Hedenquist, J.W., 1983. Characteristics of Broadlands - Ohaaki water chemistry, and changes subsequent to initial production. In: Proceedings of the New Zealand Geothermal Workshop.

Hedenquist, J.W., 1990. The thermal and geochemical structure of the broadlands-ohaaki geothermal system, new zealand. Geothermics 19 (2), 151–185.

Heise, W., Caldwell, T.G., Bertrand, E.A., Hill, G.J., Bennie, S.L., Palmer, N.G., 2016. Imaging the deep source of the Rotorua and Waimangu geothermal fields, Taupo Volcanic Zone, New Zealand. J. Volcanol. Geotherm. Res. 314, 39–48.

Heise, W., Caldwell, T.G., Bibby, H.M., Bannister, S.C., 2008. Three-dimensional modelling of magnetotelluric data from the Rotokawa geothermal field, Taupo Volcanic Zone, New Zealand. Geophys. J. Int. 173 (2), 740–750.

Horstmann, M., Sun, K., Berger, P., Olsen, P.A., Omeragic, D., Crary, S., Griffiths, R., Abubakar, A., 2015. Resistivity anisotropy and formation dip evaluation in vertical and low angle wells using LWD directional electromagnetic measurements. In: Proceedings of the SPWLA 56th Annual Logging Symposium: SPWLA-2015-LLLL.

Hou, J., Donderici, B., Torres, D., 2016. Enhanced real-time determination of resistivity anisotropy and dip using multifrequency and multicomponent induction logging. Interpretation 4 (2), SF137–SF149.

Ikhwan, M., Wallis, I.C., Rowland, J.V., 2020. Geological model and permeability framework of Bukit Daun Geothermal Field, Indonesia. In: Proceedings of the New Zealand Geothermal Workshop. Waitangi, New Zealand.

Intani, R.G., Golla, G.U., Syaffitri, Y., Paramitasari, H.M., Nordquist, G.A., Nelson, C., Ginanjar, Giri, G.K.D.S., Sugandhi, A., 2020. Improving the conceptual understanding of the Darajat Geothermal Field. Geothermics 83, 101716.

Ishibashi, T., Watanabe, N., Hirano, N., Okamoto, A., Tsuchiya, N., 2015. Beyond-laboratory-scale prediction for channeling flows through subsurface rock fractures with heterogeneous aperture distributions revealed by laboratory evaluation. J. Geophys. Res. Solid Earth 120 (1), 106–124.

Ishizu, K., Ogawa, Y., Nunohara, K., Tsuchiya, N., Ichiki, M., Hase, H., Kanda, W., Sakanaka, S., Honkura, Y., Hino, Y., Seki, K., Tseng, K.H., Yamaya, Y., Mogi, T., 2022. Estimation of spatial distribution and fluid fraction of a potential supercritical Geothermal reservoir by magnetotelluric data: a case study from Yuzawa Geothermal Field, NE Japan. J. Geophys. Res. Solid Earth 127 (2), e2021JB022911.

Jolie, E., Scott, S., Faulds, J., Chambefort, I., Axelsson, G., Gutiérrez-Negrín, L.C., Regenspurg, S., Ziegler, M., Ayling, B., Richter, A., Zemedkun, M.T., 2021. Geological controls on geothermal resources for power generation. Nat. Rev. Earth Environ. 2 (5), 324–339.

Jylhänkangas, S., 2024. Comparing Theoretical With Measured Seismic Anisotropy in the Central Taupō Volcanic Zone. Victoria University of Wellington. MSc.

Kaya, E., O'Sullivan, M.J., Yeh, A., 2014. Three-dimensional model of the deep geothermal resources in the Taupo–Reporoa Basin, New Zealand. J. Volcanol. Geotherm. Res. 284, 46–60.

Kim, Y.-S., Sanderson, D.J., 2005. The relationship between displacement and length of faults: a review. Earth. Sci. Rev. 68 (3), 317–334.

Kirkby (2026). Code and data used in "direction-dependent permeability and resistivity of fractured rocks tuned to New Zealand geothermal reservoirs". 10.5281/zenodo.18307615.

Kirkby, A., Heinson, G., 2017. Three-dimensional resistor network modeling of the resistivity and permeability of fractured rocks. J. Geophys. Res. Solid Earth 122 (4), 2653–2669.

Kirkby, A., Heinson, G., Krieger, L., 2016. Relating permeability and electrical resistivity in fractures using random resistor network models. J. Geophys. Res. Solid Earth 121 (3), 1546–1564.

Kissling, W.M., Massiot, C., 2023. Modelling of flow through naturally fractured geothermal reservoirs, Taupō Volcanic Zone, New Zealand. Geotherm. Energy 11 (1), 20.

Lane Jr, J.W., Haeni, F.P., Watson, W.M., 1995. Use of a square-array direct-current resistivity method to detect fractures in crystalline bedrock in New Hampshire. Groundwater 33 (3), 476–485.

Lee, B., Unsworth, M., Árnason, K., Cordell, D., 2020. Imaging the magmatic system beneath the Krafla geothermal field, Iceland: a new 3-D electrical resistivity model from inversion of magnetotelluric data. Geophys. J. Int. 220 (1), 541–567.

Leveridge, R.M., 2010. New resistivity-logging tool helps resolve problems of anisotropy, shoulder-bed effects. J. Pet. Technol. 62 (08), 20–22.

Light, T.S., Licht, S., Bevilacqua, A.C., Morash, K.R., 2005. The fundamental conductivity and resistivity of water. Electrochem. Solid-State Lett. 8 (1), E16.

LINZ (2012). NZ 8m digital elevation model. Land Information New Zealand. https://data.linz.govt.nz/layer/51768-nz-8m-digital-elevation-model-2012/.

Liotta, D., Brogi, A., Árnadóttir, S., Ágústsson, K., Thorsteinsdóttir, U., 2021. Field evidence of the interplay between rift and transform structures in the Krafla geothermal area, N-Iceland. Geothermics 91, 102039.

Martí, A., 2014. The role of electrical anisotropy in magnetotelluric responses: from modelling and dimensionality analysis to inversion and interpretation. Surv. Geophys. 35 (1), 179–218.

Massiot, C., Milicich, S.D., Jylhänkangas, S., Mortimer, N., Morgenstern, R., Chambefort, I., 2025. Multi-scale controls on veining in New Zealand greywacke basement rocks: implications for geothermal fluid circulation. N. Z. J. Geol. Geophys. 68 (3), 399–420. https://doi.org/10.1080/00288306.2025.2488416.

Massiot, C., Milicich, S.D., Sepulveda, F., Sophy, M.J., Lawrence, M.J.F., Griffin, A.G., Rickman, M., Carson, L.B., Rosenberg, M., Simpson, M., 2023. Highlights of borehole imaging, Tauhara geothermal field drilling, New Zealand. In: Proceedings of the 45th New Zealand Geothermal Workshop, 15-17 November 2023.

Massiot, C., Nicol, A., McNamara, D.D., Townend, J., 2017. Evidence for tectonic, lithologic, and thermal controls on fracture system geometries in an andesitic high-temperature geothermal field. J. Geophys. Res. Solid Earth 122 (8), 6853–6874.

Matsuki, K., Chida, Y., Sakaguchi, K., Glover, P.W.J., 2006. Size effect on aperture and permeability of a fracture as estimated in large synthetic fractures. Int. J. Rock Mech. Min. Sci. 43 (5), 726–755.

MBIE, 2025. From the Ground Up: A Draft Strategy to Unlock New Zealand's Geothermal Potential New Zealand. Ministry of Business, Innovation and Employment.

McNamara, D.D., Massiot, C., Lewis, B., Wallis, I.C., 2015. Heterogeneity of structure and stress in the Rotokawa Geothermal Field, New Zealand. J. Geophys. Res. Solid Earth 120 (2), 1243–1262.

McNamara, D.D., Milicich, S.D., Massiot, C., Villamor, P., McLean, K., Sépulveda, F., Ries, W.F., 2019. Tectonic controls on Taupo volcanic zone geothermal expression: insights from Te Mihi, Wairakei Geothermal field. Tectonics 38 (8), 3011–3033.

McNamara, D.D., Sewell, S., Buscarlet, E., Wallis, I.C., 2016. A review of the Rotokawa Geothermal Field, New Zealand. Geothermics 59, 281–293.

Milicich, S.D., Bardsley, C., Bignall, G., Wilson, C.J.N., 2014. 3-D interpretative modelling applied to the geology of the Kawerau geothermal system, Taupo Volcanic Zone, New Zealand. Geothermics 51, 344–350.

Milicich, S.D., Chambefort, I., Wilson, C.J.N., Alcaraz, S., Ireland, T.R., Bardsley, C., Simpson, M.P., 2020. A zircon U-Pb geochronology for the Rotokawa geothermal system, New Zealand, with implications for Taupō Volcanic Zone evolution. J. Volcanol. Geotherm. Res. 389, 106729.

Milicich, S.D., Massiot, C., Murphy, B., 2023. Fracture permeability in basement greywacke for supercritical drilling planning. In: Proceedings of the 45th New Zealand Geothermal Workshop. Auckland, New Zealand.

Morgenstern, R., Litchfield, N.J., Langridge, R.M., Heron, D.W., Townsend, D.B., Villamor, P., Barrell, D.J.A., Ries, W.F., Van Dissen, R.J., Clark, K.J., Coffey, G.L., Zoeller, A., Howell, A., Easterbrook-Clarke, L.H., 2025. New Zealand active faults database: the high-resolution dataset v2.0. New Zealand J. Geol. Geophys. 68 (5), 955–970.

Mortensen, A.K., Egilson, Þ., Gautason, B., Árnadóttir, S., Guðmundsson, Á., 2014. Stratigraphy, alteration mineralogy, permeability and temperature conditions of well IDDP-1, Krafla, NE-Iceland. Geothermics 49, 31–41.

Mroczek, E.K., Milicich, S.D., Bixley, P.F., Sepulveda, F., Bertrand, E.A., Soengkono, S., Rae, A.J., 2016. Ohaaki geothermal system: refinement of a conceptual reservoir model. Geothermics 59, 311–324.

Mroczek, S., Savage, M.K., Hopp, C., Sewell, S.M., 2020. Anisotropy as an indicator for reservoir changes: example from the Rotokawa and Ngatamariki geothermal fields, New Zealand. Geophys. J. Int. 220 (1), 1–17.

Muraoka, H., Uchida, T., Sasada, M., Yagi, M., Akaku, K., Sasaki, M., Yasukawa, K., Miyazaki, S.-I., Doi, N., Saito, S., Sato, K., Tanaka, S., 1998. Deep geothermal resources survey program: igneous, metamorphic and hydrothermal processes in a well encountering 500°C at 3729 m depth, Kakkonda, Japan. Geothermics 27 (5), 507–534.

Nemoto, K., Watanabe, N., Hirano, N., Tsuchiya, N., 2009. Direct measurement of contact area and stress dependence of anisotropic flow through rock fracture with heterogeneous aperture distribution. Earth Planet. Sci. Lett. 281 (1), 81–87.

Nicholl, M.J., Rajaram, H., Glass, R.J., Detwiler, R., 1999. Saturated flow in a single fracture: evaluation of the Reynolds equation in measured aperture fields. Water Resour. Res. 35 (11), 3361–3373.

Nicol, A., Walsh, J., Berryman, K., Villamor, P., 2006. Interdependence of fault displacement rates and paleoearthquakes in an active rift. Geology 34 (10), 865–868.

O'Sullivan, J., Gravatt, M., Riffault, J., Renaud, T., O'Sullivan, M., Ruiz, N.C., Ayling, B., Mannington, W., 2025. An updated model of Ohaaki geothermal field, New Zealand. Geothermics 130, 103339.

Odoh, I.B., Onwuemesi, A.G., 2009. Estimation of anisotropic properties of fractures in Presco campus of Ebonyi State University Abakaliki, Nigeria using Azimuthal resistivity survey method. J. Geol. Min. Res. 8, 172–179.

Olsson, W.A., Brown, S.R., 1993. Hydromechanical response of a fracture undergoing compression and shear. Int. J. Rock Mech. Min. Sci. Geomech. Abs. 30 (7), 845–851.

Pearson-Grant, S.C., Bertrand, E.A., 2021. Topography as a major influence on geothermal circulation in the Taupo Volcanic Zone, New Zealand. Geophys. Res. Lett. 48 (8), e2020GL092248.

Rajput, V., Kaya, E., Lynne, B., Altar, D.E., 2024. Reactive transport modelling of NCG-reinjection at Ngawha geothermal field. In: Proceedings of the 46th New Zealand Geothermal Workshop. Auckland, New Zealand.

Reeves, R., Pederson, J.B., 2023. Insights into the Waiotapu Geothermal Field using high resolutions SkyTEM data. In: Proceedings of the New Zealand Geothermal Workshop, 2023.

Revil, A., Glover, P.W.J., 1998. Nature of surface electrical conductivity in natural sands, sandstones, and clays. Geophys. Res. Lett. 25 (5), 691–694.

Robertson, K., Thiel, S., Meqbel, N., 2020. Quality over quantity: on workflow and model space exploration of 3D inversion of MT data. Earth Planets Space 72 (1), 1–22.

Rosenberg, M., 2017. Volcanic and Tectonic Perspectives on the Age and Evolution of the Wairakei-Tauhara Geothermal System. Victoria University of Wellington. PhD.

Rowland, J.V., Simmons, S.F., 2012. Hydrologic, magmatic, and tectonic controls on hydrothermal flow, Taupo Volcanic Zone, New Zealand: implications for the formation of epithermal vein deposits. Econom. Geol. 107 (3), 427–457.

Rucker, D.F., Fink, J.B., Loke, M.H., 2011. Environmental monitoring of leaks using time-lapsed long electrode electrical resistivity. J. Appl. Geophys. 74 (4), 242–254.

Sawayama, K., Ishibashi, T., Jiang, F., Tsuji, T., 2023. Relationship between permeability and resistivity of sheared rock fractures: the role of tortuosity and flow path percolation. Geophys. Res. Lett. 50 (20), e2023GL104418.

Sawayama, K., Ishibashi, T., Jiang, F., Tsuji, T., Fujimitsu, Y., 2021a. Relating hydraulic–electrical–elastic properties of natural rock fractures at elevated stress and associated transient changes of fracture flow. Rock. Mech. Rock. Eng. 54 (5), 2145–2164.

Sawayama, K., Ishibashi, T., Jiang, F., Tsuji, T., Nishizawa, O., Fujimitsu, Y., 2021b. Scale-independent relationship between permeability and resistivity in mated fractures with natural rough surfaces. Geothermics 94, 102065.

Scott, S., Driesner, T., Weis, P., 2016. The thermal structure and temporal evolution of high-enthalpy geothermal systems. Geothermics 62, 33–47.

Seebeck, H., Nicol, A., Villamor, P., Ristau, J., Pettinga, J., 2014. Structure and kinematics of the Taupo Rift, New Zealand. Tectonics 33 (6), 1178–1199.

Seebeck, H., Van Dissen, R., Litchfield, N., Barnes, P.M., Nicol, A., Langridge, R., Barrell, D.J.A., Villamor, P., Ellis, S., Rattenbury, M., Bannister, S., Gerstenberger, M., Ghisetti, F., Sutherland, R., Hirschberg, H., Fraser, J., Nodder, S. D., Stirling, M., Humphrey, J., Bland, K.J., Howell, A., Mountjoy, J., Moon, V., Stahl, T., Spinardi, F., Townsend, D., Clark, K., Hamling, I., Cox, S., de Lange, W., Wopereis, P., Johnston, M., Morgenstern, R., Coffey, G., Eccles, J.D., Little, T., Fry, B., Griffin, J., Townend, J., Mortimer, N., Alcaraz, S., Massiot, C., Rowland, J.V., Muirhead, J., Upton, P., Lee, J., 2024. The New Zealand community fault model – version 1.0: an improved geological foundation for seismic hazard modelling. New Zealand J. Geol. Geophys. 67 (2), 209–229.

Sharifzadeh, M., Mitani, Y., Esaki, T., 2008. Rock joint surfaces measurement and analysis of aperture distribution under different normal and shear loading using GIS. Rock. Mech. Rock. Eng. 41 (2), 299–323.

Sibson, R.H., 2000. Fluid involvement in normal faulting. J. Geodyn. 29 (3), 469–499.

Simmons, S.F., Browne, P.R.L., 2000. Hydrothermal minerals and precious metals in the broadlands-Ohaaki geothermal system: implications for understanding low-sulfidation epithermal environments. Econom. Geol. 95 (5), 971–999.

Siratovich, P.A., Heap, M.J., Villenueve, M.C., Cole, J.W., Reuschlé, T., 2014. Physical property relationships of the Rotokawa Andesite, a significant geothermal reservoir rock in the Taupo Volcanic Zone, New Zealand. Geotherm. Energy 2 (1), 10.

Tateishi, Y., Itoi, R., Tanaka, T., Takayama, J., 2015. Natural-state modeling of geothermal reservoir at Ogiri, Japan using iTOUGH2. In: Proceedings of the Fortieth Workshop on Geothermal Reservoir Engineering. Stanford, California. Stanford University.

Ucok, H., Ershaghi, I., Olhoeft, G.R., 1980. Electrical resistivity of geothermal brines. J. Pet. Technol. 32 (04), 717–727.

van Driel, M., Renaud, T., Gravatt, M., O'Sullivan, M.J., O'Sullivan, J., Riffault, J., Croucher, A., van de Vosse, F.N., Ruiz, N.C., 2023. Numerical modelling of tracer tests in the Ohaaki geothermal system. In: Proceedings of the 45th New Zealand Geothermal Workshop. Auckland, New Zealand.

Vidal, J., Genter, A., Schmittbuhl, J., 2016. Pre- and post-stimulation characterization of geothermal well GRT-1, Rittershoffen, France: insights from acoustic image logs of hard fractured rock. Geophys. J. Int. 206 (2), 845–860.

Villamor, P., Berryman, K.R., Ellis, S.M., Schreurs, G., Wallace, L.M., Leonard, G.S., Langridge, R.M., Ries, W.F., 2017. Rapid evolution of subduction-related continental intraarc rifts: the Taupo Rift, New Zealand. Tectonics 36 (10), 2250–2272.

Wallis, I.C., 2023. The Geologic Controls on Geothermal Fluid Flux at the District-, Reservoir-, and Wellbore-Scale. University of Auckland. PhD.

Wallis, I.C., McCormick, S., Sewell, S., Boseley, C., 2009. Formation assessment in geothermal using wireline tools - application and early results from the Ngatamariki geothermal field, New Zealand. In: Proceedings of the New Zealand Geothermal Workshop. Rotorua.

Wallis, I.C., McNamara, D.D., Rowland, J.V., Massiot, C., 2012. The nature of fracture permeability in the basement greywacke at Kawerau Geothermal Field, New Zealand. In: Proceedings of the Thirty-Seventh Workshop on Geothermal Reservoir Engineering. Stanford University Stanford, CA.

Wang, L., Wu, Z.-G., Fan, Y.-R., Huo, L.-Z., 2020. Fast anisotropic resistivities inversion of logging-while-drilling resistivity measurements in high-angle and horizontal wells. Appl. Geophys. 17 (3), 390–400.

Wannamaker, P.E., 2005. Anisotropy versus heterogeneity in continental solid earth electromagnetic studies: fundamental response characteristics and implications for physicochemical State. Surv. Geophys. 26 (6), 733–765.

Watanabe, N., Hirano, N., Tsuchiya, N., 2008. Determination of aperture structure and fluid flow in a rock fracture by high-resolution numerical modeling on the basis of a flow-through experiment under confining pressure. Water. Resour. Res. 44 (6), 1–11.

Watanabe, N., Hirano, N., Tsuchiya, N., 2009. Diversity of channeling flow in heterogeneous aperture distribution inferred from integrated experimental-numerical analysis on flow through shear fracture in granite. J. Geophys. Res. Solid Earth 114 (B4), 1–17.

Watanabe, N., Mogi, T., Yamaya, Y., Kitamura, K., Asanuma, H., Tsuchiya, N., 2022. Electrical conductivity of H2O-NaCl fluids under supercritical geothermal conditions and implications for deep conductors observed by the magnetotelluric method. Geothermics 101, 102361.

Wenning, Q.C., Madonna, C., Kurotori, T., Pini, R., 2019. Spatial mapping of fracture aperture changes with shear displacement using X-ray computerized tomography. J. Geophys. Res. Solid Earth 124 (7), 7320–7340.

Wilson, C.J.N., Houghton, B.F., McWilliams, M.O., Lanphere, M.A., Weaver, S.D., Briggs, R.M., 1995. Volcanic and structural evolution of Taupo Volcanic Zone, New Zealand: a review. J. Volcanol. Geotherm. Res. 68 (1), 1–28.

Wilson, C.J.N., Rowland, J.V., 2016. The volcanic, magmatic and tectonic setting of the Taupo Volcanic Zone, New Zealand, reviewed from a geothermal perspective. Geothermics 59, 168–187.

World Health Organisation (2023). Guidelines For Drinking-Water Quality: Fourth Edition Incorporating the First and Second Addenda.

Wyering, L.D., Villeneuve, M.C., Wallis, I.C., Siratovich, P.A., Kennedy, B.M., Gravley, D. M., Cant, J.L., 2014. Mechanical and physical properties of hydrothermally altered rocks, Taupo Volcanic Zone, New Zealand. J. Volcanol. Geotherm. Res. 288, 76–93.

Yamaya, Y., Suzuki, Y., Murata, Y., Okamoto, K., Watanabe, N., Asanuma, H., Hase, H., Ogawa, Y., Mogi, T., Ishizu, K., Uchida, T., 2022. 3-D resistivity imaging of the supercritical geothermal system in the Sengan geothermal region, NE Japan. Geothermics 103, 102412.

Yeboah-Forson, A., Whitman, D., 2014. Electrical resistivity characterization of anisotropy in the Biscayne Aquifer. Groundwater 52 (5), 728–736.

Zhang, Y.-Y., Liu, D.-J., Ai, Q.-H., Qin, M.-J., 2014. 3D modeling and inversion of the electrical resistivity tomography using steel cased boreholes as long electrodes. J. Appl. Geophys. 109, 292–300.